

MOLECULAR GAS **DYNAMICS KINEMATICS** OF THE STRONGLY-LENSED QUASAR HOST GALAXY RXS J1131–1231

T. K. DAISY LEUNG, DOMINIK A. RIECHERS, AND RICCARDO PAVESI

Department of Astronomy, Space Sciences Building, Cornell University, Ithaca, NY 14853, USA; tleung@astro.cornell.edu

To be submitted to the ApJ

ABSTRACT

We report observations of CO($J=2 \rightarrow 1$) and CO($J=3 \rightarrow 2$) line emission towards the quadruply-lensed quasar RXS J1131–1231 at $z=0.654$ obtained using the Plateau de Bure Interferometer (PdBI) and the Combined Array for Research in Millimeter-wave Astronomy (CARMA). Our lens modeling shows that the asymmetry in the double-horned CO($J=2 \rightarrow 1$) line profile is mainly a result of differential lensing, where the magnification factor varies from ~ 3 to ~ 9 across different kinematic components. The intrinsically symmetric line profile with a conspicuous source-plane velocity gradient suggests that the host galaxy is an extended rotating disk, with a CO size of $R_{\text{CO}} \sim 6$ kpc and a dynamical mass of $M_{\text{dyn}} \sim 8 \times 10^{10} M_{\odot}$. In addition, we find a secondary CO-emitting source near RXS J1131–1231 whose location is consistent with the optically-faint companion reported in previous studies. The lensing-corrected molecular gas masses are $M_{\text{gas}} \sim 1.4 \times 10^{10} M_{\odot}$ and $\sim 2 \times 10^9 M_{\odot}$ for RXS J1131–1231 and the companion, respectively. The gas mass fraction of $\sim 19\%$ $\sim 18\%$ inferred for RXS J1131–1231 is consistent with the trend of decreasing molecular gas fraction since $z \sim 2$ reported in recent studies. We find lensing-corrected stellar and dust masses, an IR luminosity, and a star formation rate of $M_{*} \sim 3 \times 10^{10} M_{\odot}$, $M_{\text{dust}} \sim 43 \times 10^8 M_{\odot}$, $L_{\text{IR}} \sim 1.5 \times 10^{12} L_{\odot}$, and $\text{SFR}_{\text{FIR}} \sim 120 M_{\odot} \text{ yr}^{-1}$ for RXS J1131–1231. The source-plane morphologies of its gas and stellar populations indicate that the star-formation activity may be as extended as the molecular gas reservoir. We find a $M_{\text{BH}}/M_{\text{bulge}}$ ratio of $\geq 0.27^{+11}_{-8}\%$ $> 0.27^{+0.11}_{-0.08}\%$ which is higher than the local value, suggesting that the bulk of the black hole mass of RXSJ1131-1231 is largely in place while its stellar bulge is still assembling.

Subject headings: infrared: galaxies – galaxies: high-redshift – galaxies: ISM – galaxies: evolution – quasars: individual (RXS J1131–1231) – radio lines: ISM

1. INTRODUCTION

Many recent studies of galaxy evolution have been focused on investigating the interplay between star formation and active galactic nucleus (AGN) activity across cosmic epochs (e.g., Di Matteo et al. 2005; Alexander et al. 2005; Hopkins et al. 2006; Coppin et al. 2008; Page et al. 2012; Simpson et al. 2012; Lamastra et al. 2013). It is currently not well-understood when and how the super-massive black holes (SMBHs) and stellar populations of present-day massive galaxies were assembled, but it is clear that the co-moving star formation rate and the black hole accretion rate densities both increased substantially since $z > 3$ and reached their climax at $z \sim 2$, followed by a rapid decline toward $z \sim 0$ (e.g., Hopkins & Beacom 2006; Madau & Dickinson 2014). A leading explanation for this decline is the decrease in molecular gas content and star formation efficiency (e.g., Erb et al. 2006; Carilli & Walter 2013; Walter et al. 2014), but direct molecular gas measurements at intermediate redshift ($0.2 < z < 1$) that could confirm this explanation remain largely limited to spatially unresolved CO observations of a modest sample of ~ 30 ultra-luminous infrared galaxies (ULIRGs; Combes et al. 2011, 2013).

Meanwhile, empirical scaling relations such as the $M_{\text{BH}}-M_{\text{bulge}}$ relation (e.g., Magorrian et al. 1998; Häring & Rix 2004) have been established locally, suggesting a co-eval growth between local SMBHs and their host galax-

ies. Attempts to extend this relation out to higher redshifts, beyond the peak epoch of star formation and AGN activity, have been made in recent years. These studies find that high- z AGN host galaxies do not appear to follow the same $M_{\text{BH}}-M_{\text{bulge}}$ relation as nearby spheroidal galaxies. (e.g., Walter et al. 2004; Borys et al. 2005; McLure et al. 2006; Peng et al. 2006; Riechers et al. 2008; Coppin et al. 2008; Alexander et al. 2008). Yet, the $M_{\text{BH}}-M_{\text{bulge}}$ relation remains poorly-constrained at intermediate redshifts due to the difficulty in separating the stellar component contributing to the optical emission from that of the bright AGN. This stems from the limited resolving power, which restricts the dynamic range that can be achieved at positions near the AGN. Strong gravitational lensing provides the magnification necessary to spatially separate the AGN emission from the host galaxy stellar emission, significantly improving the dynamic range that can be achieved in studies of their host galaxies with current instruments.

The quasar RXS J113151.62–123158 (hereafter RXJ1131) at $z_{\text{s, QSO}}=0.685$ (Sluse et al. 2003, hereafter S03) is a particularly well-suited source for studying the evolution of molecular gas properties in quasar host galaxies and the connection between SMBHs and their host galaxies at intermediate redshift given its unique lensing configuration. The stellar emission in the host galaxy of RXJ1131 is lensed into an Einstein ring of $1''.83$ in radius that is clearly separated from the quadruply

imaged quasar emission (Claeskens et al. 2006, hereafter C06). The foreground lens is an elliptical galaxy at $z_L = 0.295$ (S03). Reis et al. (2014) report a high spin parameter of $a \sim 0.9$ for the moderate-mass black hole in RXJ1131 ($M_{\text{BH}} = 8 \times 10^7 M_\odot$; Sluse et al. 2012), with an intrinsic bolometric luminosity of $L_{\text{bol,X}} = 1.3 \times 10^{45}$ ergs s^{-1} (Pooley et al. 2007).

In this paper, we present $\text{CO}(J=2 \rightarrow 1)$ and $\text{CO}(J=3 \rightarrow 2)$ line observations and broadband photometry spanning rest-frame UV to radio wavelengths towards RXJ1131 to study the properties of its molecular gas, dust and stellar populations. In §2, we outline details of the observations and of our data reduction procedures. In §3, we report results for the $\text{CO}(J=2 \rightarrow 1)$ and $\text{CO}(J=3 \rightarrow 2)$ emission and broadband photometry in RXJ1131. In §4, we present lens modeling and dynamical modeling of the $\text{CO}(J=2 \rightarrow 1)$ data and spectral energy distribution (SED) modeling of the photometric data. In §5, we discuss the ISM properties of the host galaxy of RXJ1131 and compare them to other galaxy populations at low and high redshift. Finally, we summarize the main results and present our conclusions in §6. We use a concordance ΛCDM cosmology throughout this paper, with parameters from the WMAP9 results: $H_0 = 69.32$ $\text{km s}^{-1} \text{Mpc}^{-1}$, $\Omega_M = 0.29$, and $\Omega_\Lambda = 0.71$ (Hinshaw et al. 2013).

2. OBSERVATIONS

2.1. PdBI $\text{CO}(J=2 \rightarrow 1)$

Observations of the $\text{CO}(J=2 \rightarrow 1)$ rotational line ($\nu_{\text{rest}} = 230.53800$ GHz) ~~at the $\nu_{\text{LO}} = 139.256$ GHz~~ **at the tuning frequency of $\nu_{\text{obs}} = 139.256$ GHz** were carried out using IRAM Plateau de Bure Interferometer (PdBI; Program ID: S14BX; PI: D. Riechers). Two observing runs were carried out on 2014 December 06 and 2015 February 05 under good weather conditions in the C and D array configurations, respectively. This resulted in 3.75 hours of cumulative six antenna-equivalent on-source time after discarding unusable visibility data. The 2 mm receivers were used to cover the redshifted $\text{CO}(J=2 \rightarrow 1)$ line and the underlying continuum emission, employing a correlator setup that provides an effective bandwidth of 3.6 GHz (dual polarization) and a native spectral resolution of 1.95 MHz ($\sim 4.2 \text{ km s}^{-1}$). The nearby quasars B1127–145 and B1124–186 were observed every 22 minutes for pointing, secondary amplitude, and phase calibration, and B1055+018 was observed as the bandpass calibrator for both tracks. MWC349 and 3C279 were observed as primary flux calibrators for the C and D array observations, respectively, yielding calibration accuracy better than 15%.

The GILDAS package was used to calibrate and analyze the visibility data. The calibrated visibility data were imaged and deconvolved using the CLEAN algorithm with “natural” weighting. This yields a synthesized clean beam size of $4''.44 \times 1''.95$ (PA = 13°). The final rms noise is $\sigma = 1.45 \text{ mJy beam}^{-1}$ over 10 MHz (21.5 km s^{-1}). The continuum image at $\nu_{\text{cont}} \sim 139$ GHz is produced by averaging

over 3.16 GHz of line-free bandwidth. This yields an rms noise of $0.082 \text{ mJy beam}^{-1}$.

2.2. CARMA $\text{CO}(J=3 \rightarrow 2)$

Observations of the $\text{CO}(J=3 \rightarrow 2)$ rotational line in RXJ1131 (~~$\nu_{\text{rest}} = 345.79599$ GHz~~ **$\nu_{\text{rest}} = 345.79599$ GHz**) ~~redshifted to $\nu_{\text{obs}} = 209.10443$ GHz~~ **at the observe frequency of $\nu_{\text{obs}} = 209.10443$ GHz** were carried out with the Combined Array for Research in Millimeter-wave Astronomy (CARMA; Program ID: cf0098; PI: D. Riechers) in the D array configuration on 2014 February 02 under poor 1.5 mm weather conditions and on 2014 February 17 under good 1.5 mm weather conditions. This resulted in a total on-source time of 2.94 hours after flagging poor visibility data. The correlator setup provides a bandwidth of 3.75 GHz in each sideband and a spectral resolution of 12.5 MHz ($\sim 17.9 \text{ km s}^{-1}$). The line was placed in the lower sideband with the local oscillator tuned to $\nu_{\text{LO}} \sim 216$ GHz. The radio quasars J1127–189 (first track) and 3C273 (second track) were observed every 15 minutes for pointing, amplitude, and phase calibration. Mars was observed as the primary absolute flux calibrator and 3C279 was observed as the bandpass calibrator for both tracks.

Given that the phase calibrator used for the first track was faint and was observed under poor weather conditions and that the phase calibrator used for the second track was far from our target source, the phase calibration is sub-par, with an rms scatter $\sim 50^\circ$ over a baseline length of ~ 135 m. We thus conservatively estimate a calibration accuracy of $\sim 40\%$ based on the flux scale uncertainties, the gain variations over time, and the phase scatter on the calibrated data. We therefore treat the derived $\text{CO}(J=3 \rightarrow 2)$ line intensity with caution and ensure that our physical interpretation of this system and the conclusion of this paper do not rely on this quantity.

The MIRIAD package was used to calibrate the visibility data. The calibrated visibility data were imaged and deconvolved using the CLEAN algorithm with “natural” weighting. This yields a synthesized clean beam size of $3''.2 \times 1''.9$ (PA = 8°) for the lower sideband image cube. The final rms noise is $\sigma = 13.3 \text{ mJy beam}^{-1}$ over a channel width of 25 MHz. An rms noise of $\sigma = 0.83 \text{ mJy beam}^{-1}$ is reached by averaging over the line-free channels in both sidebands.

2.3. VLA (Archival)

Our analysis also uses archival data of the 4.885 GHz radio continuum obtained with the VLA (Program ID: AW741; PI: Wucknitz). Observations were carried out on 2008 December 29 under excellent weather conditions in the A array configuration for a total of ~ 7 hours on-source time. The C-band receivers were used with a continuum mode setup, providing a bandwidth of 50 MHz for the two IF bands with full polarization. The nearby radio quasar J1130–149 was observed every 10 minutes for pointing, amplitude, and phase calibration. J1331+305 was observed as the primary flux calibrator, and J0319+415 was observed as the bandpass calibrator, yielding $\sim 10\%$ cal-

TABLE 1
OBSERVED PROPERTIES OF RXJ1131 AND ITS
COMPANION

Parameter	Unit	Value
z_{CO}		0.6541 ± 0.0002
$I_{\text{CO}(2-1)}$	Jy km s^{-1}	20.3 ± 0.6
$S_{\text{CO}(J=2 \rightarrow 1)}$	$\text{Jy km s}^{-1} \text{ beam}^{-1}$	8.12 ± 0.30
$\text{FWHM}_{\text{CO}(2-1)}^a$	km s^{-1}	$179 \pm 9, 255 \pm 28$
$\text{FWHM}_{\text{CO}(2-1)}^b$	km s^{-1}	220 ± 72
$I_{\text{CO}(3-2)}$	Jy km s^{-1}	35.7 ± 6.9

^a From fitting a double Gaussian to the observed $\text{CO}(J=2 \rightarrow 1)$ spectrum (Figure 1).

^b From fitting a double Gaussian with a common FWHM to the de-lensed $\text{CO}(J=2 \rightarrow 1)$ spectrum (Figure 5).

ibration accuracy. We used AIPS to calibrate the visibility data. The calibrated visibility data were imaged and deconvolved using the CLEAN algorithm with robust=0, which was chosen to obtain a higher resolution image given high SNR. This yields a synthesized clean beam size of $0''.49 \times 0''.35$ (PA=0.18°) and a final rms noise of $\sigma = 13 \mu\text{Jy beam}^{-1}$.

2.4. HST (Archival)

We obtained an *HST* image taken with the ACS using the F555W filter (V-band) from the Hubble Legacy Archive. The details of the observations can be found in C06. We apply an astrometric correction to the optical image by adopting the VLA 5 GHz map as the reference coordinate frame. We shift the latter to the east by $0''.5963$ in R.A. and $+0''.8372$ in Dec., which is consistent with the typical astrometric precision ($1''$ – $2''$) of images from the Hubble Legacy Archive¹. This astrometric correction is critical to avoid artificial spatial offsets between different emitting regions and to carry out our lens modeling, in which the absolute position of the foreground lensing galaxy is based on its coordinates in the high-resolution optical image. The VLA image is calibrated using a well-monitored phase calibrator, with absolute positional accuracy of ~ 2 mas. For this reason, the absolute alignment between the VLA image and other interferometric images reported in this paper are expected to have an astrometric precision better than $0''.1$, modulo uncertainties related to the SNR and phase instability.

3. RESULTS

The observed properties of $\text{CO}(J=2 \rightarrow 1)$ and $\text{CO}(J=3 \rightarrow 2)$ emission are summarized in Table 1.

3.1. $\text{CO}(J=2 \rightarrow 1)$ Emission

We detect $\text{CO}(J=2 \rightarrow 1)$ line emission toward the background source in the PdBI data at $\gtrsim 27\sigma$ significance, **confirming the redshift at $z_{\text{CO}} = 0.6537 \pm 0.0005$, enabling us to constrain its redshift at $z_{\text{CO}} = 0.6541 \pm 0.0002$ ².** **The emission is spatially and dynamically resolved** The

emission is spatially and kinematically resolved with a highly asymmetric double-horned line profile as shown in Figure 1. Fitting a double Gaussian results in peak flux densities of 75.3 ± 2.6 mJy and 24.0 ± 2.0 mJy, and a FWHM of 179 ± 9 km s^{-1} and 255 ± 28 km s^{-1} for the two components, respectively. The peaks are separated by $\Delta v_{\text{sep}} = 400 \pm 12$ km s^{-1} . The total integrated line flux is **24.1 ± 2.3 Jy km s^{-1} 20.3 ± 0.6 Jy km s^{-1} .**

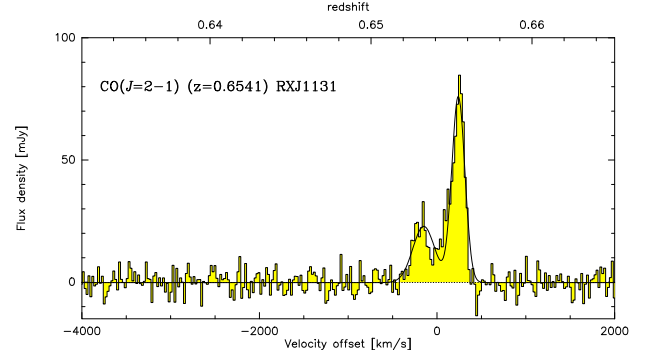


FIG. 1.— Continuum-subtracted spectrum (histogram) of $\text{CO}(J=2 \rightarrow 1)$ emission towards RXJ1131, with a spectral resolution of 21.5 km s^{-1} . The solid black line shows a double-Gaussian fit to the line profile. The velocity scale is with respect to $z=0.6537$, which is approximately the line center considering the asymmetry resulting from differential lensing. $z=0.6541$, which corresponds to the line center of RXJ1131 based on the de-lensed line profile (Figure 5). A detailed discussion of this effect is presented in §4.1.2.

We construct a zeroth order moment map, red/blue channel maps, and first and second moment maps, as shown in Figure 2, using the uv -continuum subtracted data cube over a velocity range of $\Delta v \sim 750 \text{ km s}^{-1}$. The higher-order moment maps are produced using unbinned channel maps with 3σ clipping. The peak flux density is $8.12 \pm 0.30 \text{ Jy km s}^{-1} \text{ beam}^{-1}$ in the intensity map.

The deconvolved source size FWHM obtained by fitting a two-dimensional Gaussian to the integrated line map in the image plane is $5''.1 \pm 0''.72 \times 3''.72 \pm 0''.66$, and thus, the emission is resolved over ~ 2.2 beams. While the lensed emission is not strictly distributed as a two-dimensional Gaussian; the fit recovers the line intensity enclosed by the emitting region, therefore we take this as an estimate on the full extent of the lensed emission. On the other hand, if we assume that the spatial distribution of the lensed molecular gas emission is similar to that in the optical to near-IR wavelengths, the lensed emission would be more accurately described by an annulus, enclosing the partially complete “Einstein ring” and the lensed knots (see Figure 2). The deconvolved source size FWHM from fitting a single two-dimensional Gaussian to the integrated line image yields $5''.1 \pm 0''.7 \times 3''.7 \pm 0''.7$, consistent with the results obtained by uv -plane fitting within the uncertainties. To model the complex spatial distribution of the line emission (Figure 2), we fit two independent Gaussians and find deconvolved source sizes of $3''.8 \pm 0''.4 \times 1''.9 \pm 0''.4$ and $3''.6 \pm 0''.3 \times 1''.5 \pm 0''.3$. Therefore, the emission is slightly resolved over ~ 2 beams. The lensed CO emission is unlikely to be dis-

¹ http://hla.stsci.edu/hla_faq.html

² This redshift is derived by fitting a double-Gaussian to the de-lensed spectrum, which is shown in Figure 5.

tributed as Gaussians given the morphology seen in optical and near-IR emission that were observed at higher resolution, i.e., the lensed emission of CO (without beam convolution) is more likely to have an annulus configuration enclosing a partially complete “Einstein ring” with structures along the arc and knots (see Figure 2). Nevertheless, the deconvolved source sizes and the spatially offset blue wing compared to optical emission suggest that the CO-emitting region in RXJ1131 is more extended than its stellar (and of course quasar) emission.

We also place an upper limit on HNC($J=2 \rightarrow 1$) line emission in the foreground galaxy at $z \sim 0.295$. Assuming a typical line width of 300 km s^{-1} , this corresponds to a 3σ limit of $0.35 \text{ Jy km s}^{-1} \text{ beam}^{-1}$.

3.2. CO($J=3 \rightarrow 2$) Emission

We detect CO($J=3 \rightarrow 2$) line emission towards RXJ1131 in the CARMA data at $\gtrsim 5\sigma$ significance. The spectrum is shown in Figure 3 and appears to be consistent with a double-peaked profile. We estimate a line intensity of $35.7 \pm 21.9 \text{ Jy km s}^{-1}$ **$35.7 \pm 6.9 \text{ Jy km s}^{-1}$** by summing up fluxes over the FWZI linewidth used to infer the CO($J=2 \rightarrow 1$) line intensity ($\sim 700 \text{ km s}^{-1}$). Assuming the spatial extent of CO($J=2 \rightarrow 1$) and CO($J=3 \rightarrow 2$) is similar and therefore the emission is magnified by the same amount, the measured line intensities correspond to a brightness temperature ratio of $r_{32} = T_{\text{CO}(J=3 \rightarrow 2)} / T_{\text{CO}(J=2 \rightarrow 1)} = 0.66 \pm 0.41$. ~~Taking into account the large phase errors associated with CO($J=3 \rightarrow 2$), this is consistent with~~ **0.78 ± 0.62 , where this uncertainty includes those introduced in absolute flux calibration and is dominated by the large phase errors associated with the CO($J=3 \rightarrow 2$) observations. This ratio is consistent with** thermalized excitation within the uncertainties, as commonly observed in nuclear regions of nearby ULIRGs and high- z quasars (e.g., Weiß et al. 2007; Carilli & Walter 2013), but also with the lower excitation seen in normal star-forming disks (e.g., Dannerbauer et al. 2009; Carilli & Walter 2013).

3.3. Continuum Emission

No ~~1.5 mm~~ **1.4 mm** continuum emission is detected at the position of CO($J=3 \rightarrow 2$) down to a 3σ limit of $2.49 \text{ mJy beam}^{-1}$. This is consistent with the spectrum shown in Figure 3.

We detect ~~2 mm~~ **2.2 mm** continuum emission at an integrated flux density of $1.2 \pm 0.2 \text{ mJy}$, with a peak flux of $S_\nu = 799 \pm 88 \mu\text{Jy beam}^{-1}$ centered on the lensing galaxy (Figure 4). **We note that the reported flux uncertainties do not include those from absolute flux calibration.** Slightly extended emission along the lensed arc is also detected. This suggests that we detect emission in both the foreground galaxy and the background galaxy and that the emission is marginally resolved along its major axis. We subtract a point source model in the uv -plane to remove the unresolved part of the emission, which we here assume to be dominated by the foreground galaxy. The peak emission (~~$0.39 \pm 0.08 \text{ mJy}$~~) **of**

flux $S_\nu = 0.39 \pm 0.08 \text{ mJy}$ in the residual map coincides with the lensed arc, and is consistent with the difference between the integrated and the peak flux in the original continuum map ($\sim 0.4 \text{ mJy}$). We therefore adopt ~~$S_\nu = 0.39 \pm 0.08 \text{ mJy}$~~ **$S_\nu = 0.39 \pm 0.22 \text{ mJy}$** as the 2 mm continuum flux measurement for the background galaxy (RXJ1131). ~~The quoted uncertainty is from the flux measurement in the residual map.~~ **The quoted uncertainty is solely based on the uncertainties associated with the flux density of the point source model ($\delta S_\nu = 0.088 \text{ mJy}$) and that of the integrated flux in the original data (0.2 mJy), and does not account for that in the de-blending procedure, where we have assigned 100% of the point source flux to the foreground galaxy. We report the peak flux in the original map ($S_\nu = 799 \pm 88 \mu\text{Jy beam}^{-1}$) for the foreground galaxy, which is the best estimate possible at the resolution of our observations, but we acknowledge that a non-negligible contribution from the background source to the peak flux cannot be ruled out.**

The VLA C-band continuum image in Figure 4 shows resolved emission from the jets and the core of the foreground elliptical galaxy as well as emission toward the background quasar. Multiple peaks are seen along the arc with their centroids coincident with the optical emission from the quasar. We extract the flux densities for the lensing arc and the radio core in Table 2. We find a spectral index of $\alpha_{\text{bcm}}^{2\text{mm}} = -0.024$ **0.02** for the foreground galaxy and $\alpha_{\text{bcm}}^{2\text{mm}} = -0.34$ **0.35** for the background galaxy by fitting power-laws ($S_\nu \propto \nu^\alpha$) to their continuum emission at 5 GHz and 2 mm. **The spectral slope derived for the background source is flatter than the typical slope of pure synchrotron emission ($\alpha \sim -0.7$), suggesting that a dominant fraction of the observed 2 mm emission arises from cold dust and free-free emission. This spectral slope would only be shallower if a non-negligible fraction from the background source contribute to the point source flux at 2 mm in the de-blending process. This would also explain the atypical flat spectrum found for the foreground galaxy. Assuming a synchrotron slope of $\alpha \sim -0.7$ and that the emission at 5 GHz is purely synchrotron, we find $S_{2\text{mm}} = 0.27 \pm 0.22 \text{ mJy}$ from cold dust and free-free emission in the background galaxy.**

3.4. Photometry

We compile mid-IR (MIR) to far-IR broadband photometry from various catalogs available on the NASA/IPAC Infrared Science Archive (IRSA) in Table 2 with aperture corrections when warranted. These data were obtained using the Cerro Tololo Inter-American Observatory (CTIO) for the Two Micron All Sky Survey (2MASS; Skrutskie et al. 2006), the Wide-field Infrared Survey Explorer (WISE; Wright et al. 2010), the *Infrared Astronomical Satellite* (IRAS; Neugebauer et al. 1984), and the Multi-band Imaging Photometer (MIPS; Rieke et al. 2004) and Mid-infrared Infrared Array Camera (IRAC; Fazio et al. 2004) on the *Spitzer Space Telescope*. We retrieve PBCD (level 2) *Spitzer*/IRAC images from the *Spitzer* Heritage Archive and perform aperture photometry on the channel

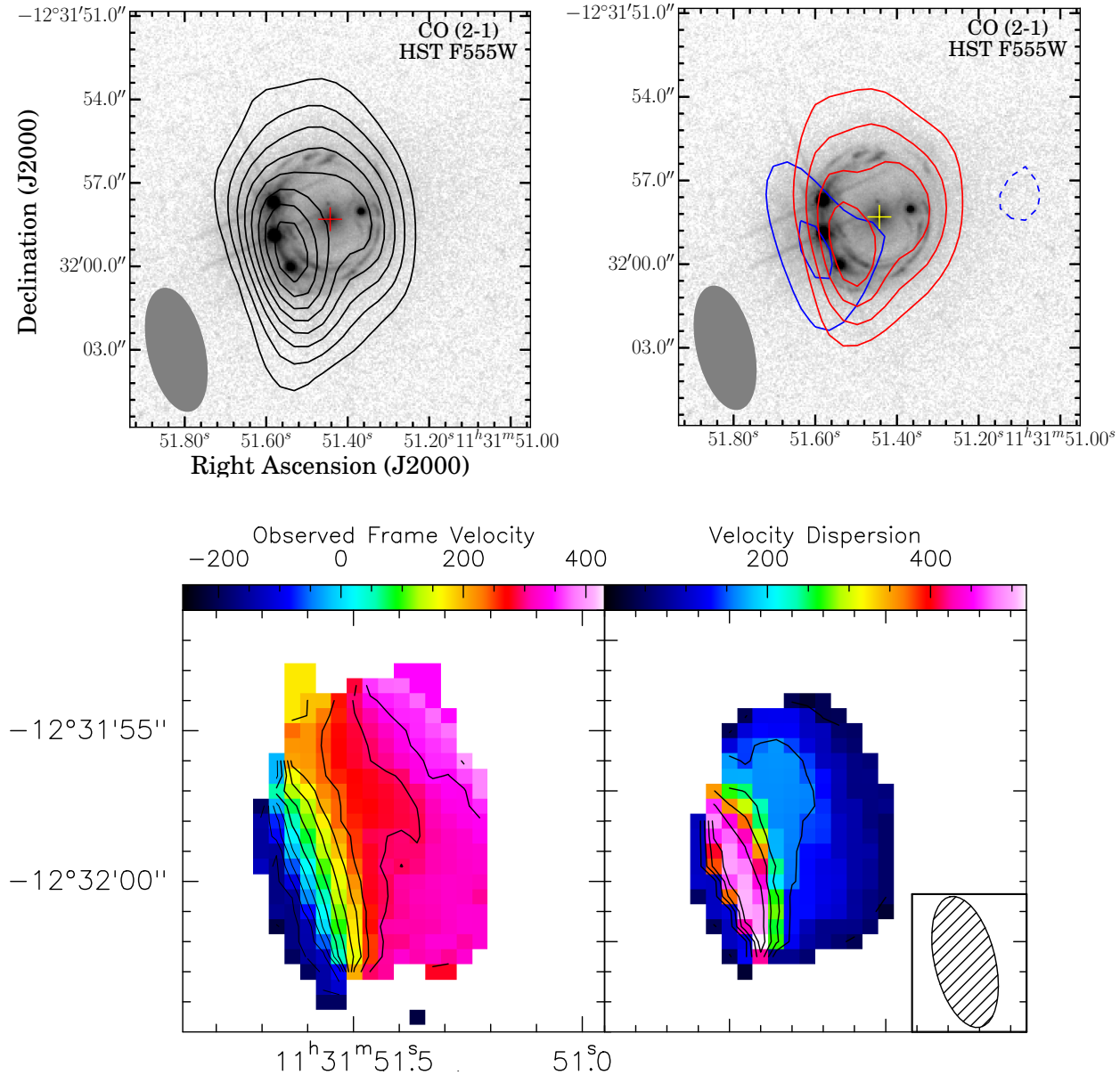


FIG. 2.— Top left: overlay of the velocity-integrated CO($J=2 \rightarrow 1$) emission on an archival *HST* V-band (F555W) image. Top right: same as top left, except the contours are color-coded to represent the red- and blueshifted emission, which are extracted by integrating over $v \in [-19, 357] \text{ km s}^{-1}$ and $v \in [-395, -19] \text{ km s}^{-1}$, respectively. The contours in both top panels start at 3σ and increment at steps of $\pm 3\sigma$, where $\sigma = 0.3 \text{ mJy beam}^{-1}$ for the top left panel, and $\sigma = 0.4 \text{ mJy beam}^{-1}$ (red) and $0.5 \text{ mJy beam}^{-1}$ (blue) for the top right panel. The crosses denote the location of the foreground galaxy at $z=0.295$. Contours for the first (bottom left) and second (bottom right) moment maps of the CO($J=2 \rightarrow 1$) line emission are shown in steps of 50 km s^{-1} , and 100 km s^{-1} , respectively. The synthesis beam size is $4''.4 \times 2''.0$, at PA = 13° .

1 image to extract the flux density at $3.6 \mu\text{m}$ since it is not available from the IRSA archive.

The emission in the IRAC images is slightly extended. We thus use an *HST* image ($\sim 0''.07$ resolution) to determine the origin of their centroids, all of which are found to be centered at the position corresponding to the lensed emission from the background galaxy. To recover the diffuse background emission, we subtract a point source model centered on the lensing galaxy, using the average FWHM found by fitting a Gaussian profile to several field stars with the IMEXAM routine of IRAF. We perform aperture photometry on the residual image to obtain decomposed flux measurements of the background galaxy. The

photometry for the foreground galaxy is then obtained by subtracting the background emission from the observed total flux. The resulting photometry in Table 2 is obtained after performing an aperture correction described in the IRAC Instrument Handbook³ to correct for the fact that the imaging was calibrated using a $12''$ aperture, which is larger than the aperture ($5''.8$) we used to perform aperture photometry.

We fit a power-law spectrum to the decomposed IRAC photometry to disentangle the background and foreground emission from the total flux observed in the MIPS $24 \mu\text{m}$

³ <http://irsa.ipac.caltech.edu/data/SPITZER/docs/irac/iracinstrumenthandbook/>

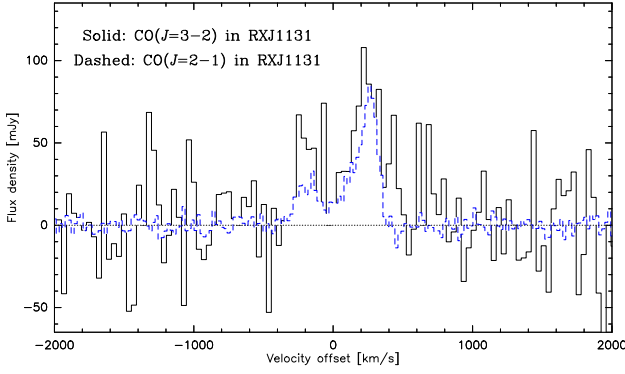


FIG. 3.— CARMA CO($J=3 \rightarrow 2$) line profile (solid) without continuum subtraction is over-plotted on the continuum-subtracted PdBI CO($J=2 \rightarrow 1$) line profile (dashed). The velocity scale is with respect to $z=0.6537$, which corresponds to the dynamical center of the CO($J=2 \rightarrow 1$) line. **$z=0.6541$, which corresponds to the line center of CO($J=2 \rightarrow 1$) line emission.** The spectral resolution for CO($J=3 \rightarrow 2$) and CO($J=2 \rightarrow 1$) is 35.8 km s^{-1} and 21.5 km s^{-1} , respectively.

band. The spectral indices corresponding to the best-fitting curves are $\alpha = -1.8$ and $\alpha = -0.85$ for the lensing galaxy and RXJ1131, respectively. The latter is consistent with the mean $3.6\text{--}8 \mu\text{m}$ spectral slope of $\alpha = -1.07 \pm 0.53$ found for unobscured AGN (Stern et al. 2005). An extrapolation of the fit to $24 \mu\text{m}$ yields $33.96 \pm 0.01 \text{ mJy}$ and $25.19 \pm 0.03 \text{ mJy}$ for the foreground galaxy and RXJ1131, respectively. The uncertainties are the standard deviations of the extrapolated fluxes obtained from two independent Monte Carlo simulations, each of 500 iterations. We incorporate the decomposed $24 \mu\text{m}$ data in our SED fitting to provide some constraints on the Wien tail beyond the dust peak of the SED of RXJ1131. Details of the SED modeling are presented in §4.5.

Extraction of the *Herschel*/SPIRE photometry at 250, 350, and $500 \mu\text{m}$ was carried out using SUSSEXTRACTOR within the Herschel Interactive Processing Environment (HIPE; Ott 2010) on Level 2 maps obtained from the Herschel Science Archive. These maps were processed by the SPIRE pipeline version 13.0 within HIPE. The SUSSEXTRACTOR task estimates the flux density from an image convolved with a kernel derived from the SPIRE beam. The flux densities measured by SUSSEXTRACTOR were confirmed by using the Timeline Fitter, which performs photometry by fitting a 2D elliptical Gaussian to the Level 1 data at the source position given by the output of SUSSEXTRACTOR. The fluxes obtained from both methods are consistent within the uncertainties.

4. ANALYSIS

4.1. Lens Modeling

At the angular resolution of the CO($J=2 \rightarrow 1$) data, the source is resolved $\gtrsim 2$ resolution elements. Given the extent of the lensed emission (see Figure 2), this implies that we do not resolve structures (e.g. knots and arcs) of the lensed emission in our CO($J=2 \rightarrow 1$) data. Nevertheless, the high spectral resolution of these data provides **dynamical kinematic** information on spatial scales smaller than the beam (see Figure 2). Hence, we reconstruct the intrinsic **dynamics line profile and source-plane velocity structure** by carrying out a parametric lens modeling over

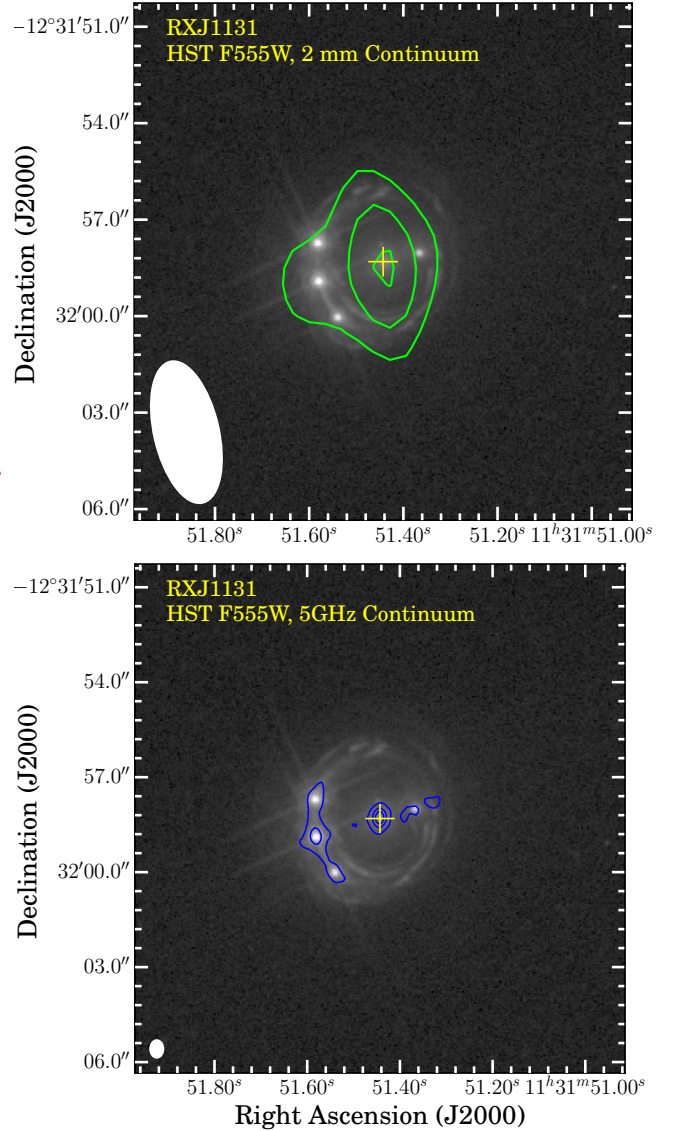


FIG. 4.— Top: overlay of the 2 mm continuum emission on the optical image. Contours start and increment at steps of $\pm 3\sigma$, where $\sigma_{2\text{mm}} = 0.082 \text{ mJy beam}^{-1}$. Bottom: overlap of the VLA 5 GHz continuum emission on the optical image. **Contours correspond to [10, 40, 60, 100] % of the peak flux density of $S_{5\text{GHz}} = 0.74 \pm 0.01 \text{ mJy}$.** The central crosses in both panels indicate the centroid of the foreground galaxy, as detected in the optical image. The synthesis beam size is $4''.4 \times 2''.0$, at PA = 13° for the PdBI observations (top), and $0''.5 \times 0''.4$ (PA = 0.18°) for the VLA observations (bottom).

different channel slices of the interferometric data using our lensing code UVMCMCFIT (Bussmann et al. 2015a; see Bussmann et al. 2015b for details of the code). Our approach follows a similar strategy as Riechers et al. (2008), who reconstruct a source-plane velocity gradient and constrain the gas dynamics in the $z > 4$ quasar host galaxy of PSS J2322+1944, which is also lensed into an Einstein ring configuration. To ensure adequate SNRs for lens modeling, we bin the frequency channels by a factor of five to produce seven independent $\Delta\nu \sim 105 \text{ km s}^{-1}$ channels (dashed line in Figure 5) that cover the full linewidth of $\sim 750 \text{ km s}^{-1}$.

We model the lens mass distribution using a singular isothermal ellipsoid (SIE) profile, which is described by

TABLE 2
PHOTOMETRY DATA

Wavelength (μm)	Frequency (GHz)	Flux Density (mJy)	Instrument
Combined/Unresolved			
1.25	239834	1.009 ± 0.09	CTIO/J-Band
1.65	181692	1.448 ± 0.12	CTIO/H-Band
2.17	138153	2.064 ± 0.16	CTIO/Ks-Band
3.4	88174.2	7.027 ± 0.14	WISE/W1
3.6	83275.7	5.618 ± 0.0021	Spitzer/IRAC
4.5	66620.5	7.803 ± 0.0021	Spitzer/IRAC
4.6	65172.3	8.872 ± 0.16	WISE/W2
5.8	51688.4	10.720 ± 0.0051	Spitzer/IRAC
8.0	37474.1	14.470 ± 0.0041	Spitzer/IRAC
12	24982.7	21.960 ± 0.42	WISE/W3
12	24982.7	< 400	IRAS
22	13626.9	55.110 ± 1.9	WISE/W4
24	12491.4	70.204 ± 0.026	Spitzer/MIPS
25	11991.7	< 500	IRAS
60	4996.54	< 600	IRAS
100	2997.92	< 1000	IRAS
250	1199.17	289.4 ± 9.6	Herschel/SPIRE
350	856.55	168.2 ± 8.6	Herschel/SPIRE
500	599.585	56.8 ± 8.8	Herschel/SPIRE
1387.93	216	< 2.492	CARMA
2152.82	139.256	1.230 ± 0.220	PdBI
Foreground Lensing Galaxy (deblended bands)			
0.555	540167	0.056 ± 0.006	HST-ACS/V-Band
0.814	368295	0.238 ± 0.013	HST-ACS/I-Band
1.6	187370	0.539 ± 0.041	HST-NICMOS(NIC2)/H-Band
3.6	83275.7	0.585 ± 0.003^a	Spitzer/IRAC
4.5	66620.5	1.794 ± 0.0027^a	Spitzer/IRAC
5.8	51688.4	3.163 ± 0.0059^a	Spitzer/IRAC
8.0	37474.1	4.589 ± 0.0057^a	Spitzer/IRAC
2152.82	139.256	0.799 ± 0.082	PdBI
61414	4.8815	0.866 ± 0.027	VLA
Background Galaxy RXJ1131 (deblended bands)			
0.555	540167	0.009 ± 0.0041^b	HST-ACS/V-Band
0.814	368295	0.041 ± 0.0054^b	HST-ACS/I-Band
1.6	187370	0.133 ± 0.004^b	HST-NICMOS(NIC2)/H-Band
3.6	83275.7	5.034 ± 0.0021	Spitzer/IRAC
4.5	66620.5	6.009 ± 0.0017	Spitzer/IRAC
5.8	51688.4	7.557 ± 0.003	Spitzer/IRAC
8.0	37474.1	9.881 ± 0.0039	Spitzer/IRAC
2152.82	139.256	0.390 ± 0.220^c	PdBI
61414	4.8815	1.273 ± 0.042	VLA

REFERENCES. — The *HST* photometry is adopted from C06.

NOTE. — The IRAC photometry for channel 1 (3.6 μm) is extracted directly from the image and from the Spitzer Heritage Archive for channels 2–4 (4.5, 5.8, and 8.0 μm). The flux uncertainties quoted for radio and mm observations (PdBI, CARMA, and VLA) do not include those from absolute flux calibration. All upper limits are 3σ .

^a Flux obtained using aperture photometry after subtracting the emission of RXJ1131 from the total emission.

^b A contribution from the quasar has been removed (see C06), and thus the flux density corresponds to the host galaxy only.

^c Flux extracted from the residual map after subtracting a point-source model. For SED modeling, we use $S_{2\text{mm}} = 0.27 \pm 0.22$ mJy to exclude synchrotron emission (see §3.3).

five free parameters: the positional offset in R.A. and Dec. relative to an arbitrary chosen fixed coordinate in the image, the Einstein radius, the axial ratio, and the position angle. Positional offset between the foreground galaxy and the pre-defined coordinate is initialized using the VLA radio continuum map. We impose a uniform prior of $\pm 0''.05$ in both $\Delta\text{R.A.}$ and $\Delta\text{Dec.}$, motivated by the astrometry uncertainties in the VLA image as well as the uncertainties provided by previous SIE lens model (C06). We initialize the Einstein radius based on the model parameters

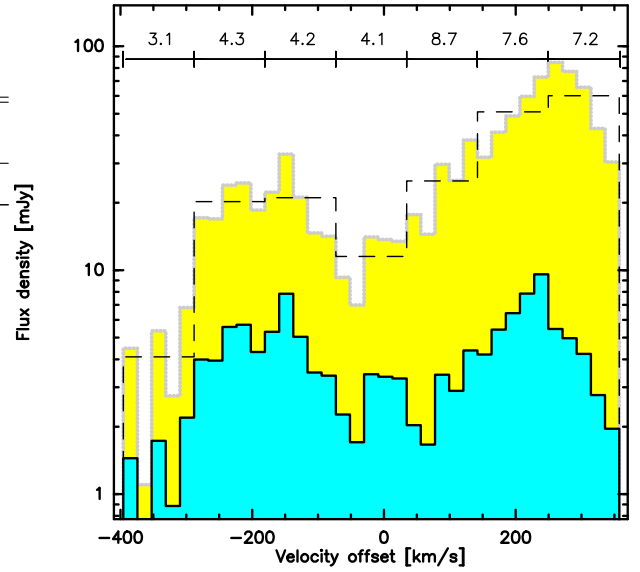


FIG. 5.— The full resolution CO($J=2 \rightarrow 1$) spectrum (yellow histogram) and the binned spectrum (dashed line) with the seven $\Delta v \sim 105 \text{ km s}^{-1}$ channels used for lens modeling. The blue histogram shows the “intrinsic” line profile of RXJ1131 after subtracting a contribution from its companion galaxy and correcting for lensing using the magnification factor μ_L as annotated by the horizontal bar shown above each respective model channel.

reported by C06 and impose a uniform prior using $\pm 3\sigma$ of their uncertainties. The sources are modeled using elliptical Gaussian profiles, which are parameterized by six free parameters: the positional offset in R.A. and Dec. relative to the lens, the intrinsic flux density, the effective radius, the axial ratio, and the position angle. The position of each source is allowed to vary between $\pm 1''.5$ (i.e., within the Einstein radius) and the effective radius is allowed to vary from $0''.01$ – $2''$.

Our code uses an Markov Chain Monte Carlo (MCMC) approach to sample the posterior probability distribution function (PDF) of the model parameters. In each model, we require a target acceptance rate of ~ 0.25 – 0.5 and check for chain convergence by inspecting trace plots and by requiring that the samples are obtained beyond at least an autocorrelation time. We thus employ $\sim 50,000$ samples as the initial “burn-in” phase to stabilize the Markov chains (which we then discard) and use the final $\sim 5,000$ steps, sampled by 128 walkers, to identify the posterior. Here, we identify the best-fit model and the quoted uncertainties using the median and the 68% confidence intervals in the marginal PDFs.

We first obtain a preliminary lens model for each channel slice independently, where their lens parameters are allowed to vary and are initialized according to the aforementioned way. We obtain the final model by repeating the modeling over each slice but fixing their lens parameters to the overall median in the preliminary models, as listed in Table 3. This ensures that all models share the same lens profile. The magnification factors in Table 4 are determined by taking the ratio between the image plane flux and the source plane flux of each model.

Our model parameters in Table 3, describing the mass distribution of the lensing galaxy, are consis-

TABLE 3
LENS PARAMETERS CONSTRAINED BY
MODELS OF SEVEN VELOCITY CHANNELS

Parameters	Median values
Offset in RA	($''$) 0.004 ± 0.027
Offset in Dec	($''$) 0.003 ± 0.027
Axial Ratio	0.56 ± 0.16
Position Angle	(deg) 103 ± 22
Einstein Radius ^a	($''$) 1.833 ± 0.002

NOTE. — Parameters describing the foreground lens are obtained based on the median in the preliminary models (see text for details). All angular offsets are with respect to $\alpha = 11^{\text{h}}31^{\text{m}}51^{\text{s}}.44$, $\delta = -12^{\circ}31'58.''3$ (J2000).

^a This corresponds to mass of $M(\theta < \theta_E) = (7.42 \pm 0.02) \times 10^{11} M_{\odot}$ within the Einstein radius.

tent (within the uncertainties) with that of the SIE model presented by C06. We find a mass of $M(\theta < \theta_E) = (7.47 \pm 0.02) \times 10^{11} M_{\odot}$ within the Einstein radius.

4.1.1. Interpretation of the Source-plane Morphology

The reconstructed source locations, as represented by magenta ellipses in Figure 6, demonstrate an intrinsic velocity gradient across the source plane, which is consistent with a kinematically-ordered disk-like galaxy. Additional support to the disk conjecture can be found in the double-horned line profile (Figure 1) and the observed (image plane) velocity field (Figure 2). Furthermore, C06 also find that the reconstructed source plane emission in optical-NIR is best-reproduced using a $n = 1$ Sersic profile. We thus interpret RXJ1131 as a disk galaxy.

A better fit is found for the lens model of the red-most channel if we add a second source component (see top left panel in Figure 6). This is consistent with previous results reported by Brewer & Lewis (2008, hereafter B08), who find an optically faint companion (component F in their paper) ~ 2.4 kpc in projection from the AGN host galaxy in V-band, and with C06, who find evidence for an interacting galaxy near RXJ1131. Spatially, the red velocity component of the CO emission also coincides with this component F. It is therefore likely that we detect CO($J = 2 \rightarrow 1$) emission in a companion galaxy.

We decompose the total line flux into two components: one from RXJ1131 and the other from its companion. Since the companion is only detected in the red-most channel, we derive its intrinsic gas mass using the best-fit flux densities and magnification factors obtained from the models of this channel. Assuming a brightness temperature ratio of $r_{21} = 1$ between CO($J = 2 \rightarrow 1$) and CO($J = 1 \rightarrow 0$) lines and a CO luminosity-to- H_2 mass conversion factor of $\alpha_{\text{CO}} = 0.8 M_{\odot} (\text{K km pc}^2)^{-1}$, we find a molecular gas mass of $M_{\text{gas}} = (1.92 \pm 0.09) \times 10^9 M_{\odot}$. For the molecular gas mass in RXJ1131, we derive its intrinsic line flux over the FWZI linewidth using the respective magnification factors listed in Table 4, which to first order takes into account the effect of differential lensing. This yields $I_{\text{CO}(J=2 \rightarrow 1)} = 2.93 \pm 0.70 \text{ Jy km s}^{-1}$, where the uncertainty includes those on the magnification factors. Adopting the same brightness temperature ratio and

TABLE 4
MAGNIFICATION FACTORS OF VARIOUS KINEMATIC
COMPONENTS IN CO($J = 2 \rightarrow 1$)

Velocity Range (km s ⁻¹)	Source 1 μ_L	Source 2 μ_L
346–260	7.2 ± 5.6	6.7 ± 2.5
238–153	7.6 ± 1.6	
131–45	8.7 ± 2.0	
24–-62	4.1 ± 0.9	
-84–-170	4.2 ± 0.6	
-191–-277	4.3 ± 2.4	
-300–-385	3.1 ± 0.9	
weighted average	4.4	
median	5.5	

NOTE. — First column corresponds to the rest-frame velocity ranges taken from the center of an unbinned channel (see Figure 5). Each row corresponds to a (binned) channel slice used for lens modeling. Source 1 is RXJ1131 and source 2 is its companion.

α_{CO} as used for the companion, this corresponds to a gas mass of $M_{\text{gas}} = (1.38 \pm 0.33) \times 10^{10} M_{\odot}$, which implies a gas mass ratio of $\sim 7:1$ between RXJ1131 and its companion.

The spatial resolution of the data in hand is a few arc-sec, which implies that despite the high SNR and spectral resolution, constraints on the intrinsic sizes of the lensed galaxies are modest, and thus the magnification factors may be under-predicted (see e.g., Bussmann et al. 2015b; Dye et al. 2015; Rybak et al. 2015).

4.1.2. Spatial Extent and Differential Lensing

In the image-plane integrated line map shown in Figure 2, the redshifted component is cospatial with the Einstein ring seen in the optical image, with most of its apparent flux originating from the lensed arc in the south-east, whereas the blue component is predominately coming from solely the lensed arc. To further illustrate this, we show the channel maps of 21.5 km s^{-1} width and a spatial spectra map of $1.''5$ resolution in Figure 7 and Figure 8, respectively. These figures show that redshifted emission is present to the west, peaking toward the lensing arc (black crosses in Figure 7), and shifts to the east with decreasing velocity (blue wing). This is consistent with the source plane positions in our models and is suggestive of an extended CO emitting region.

~~Similar to previous studies of RXJ1131, where differential lensing across the HST V-, I-, and H-bands has been detected with a magnification factor decreasing from 10.9 to 7.8 (C06), the highly asymmetric CO($J = 2 \rightarrow 1$) line profile suggests that differential lensing is also non-negligible for CO, causing the redshifted emission to be apparently much brighter than the blueshifted component. This can be explained by the difference in magnification factor (μ_L) which varies from 8.7 to 3.1 across the CO($J = 2 \rightarrow 1$) line (Table 4) and also partly due to a contribution from the companion in the redshifted velocity channels. Previous studies of RXJ1131 find evidence for differential lensing across the HST V-, I-, and H-bands, where the magnification factor varies from 10.9 to 7.8 (C06). Here, we find that the highly asymmetric CO($J = 2 \rightarrow 1$) line profile is predominantly a result~~

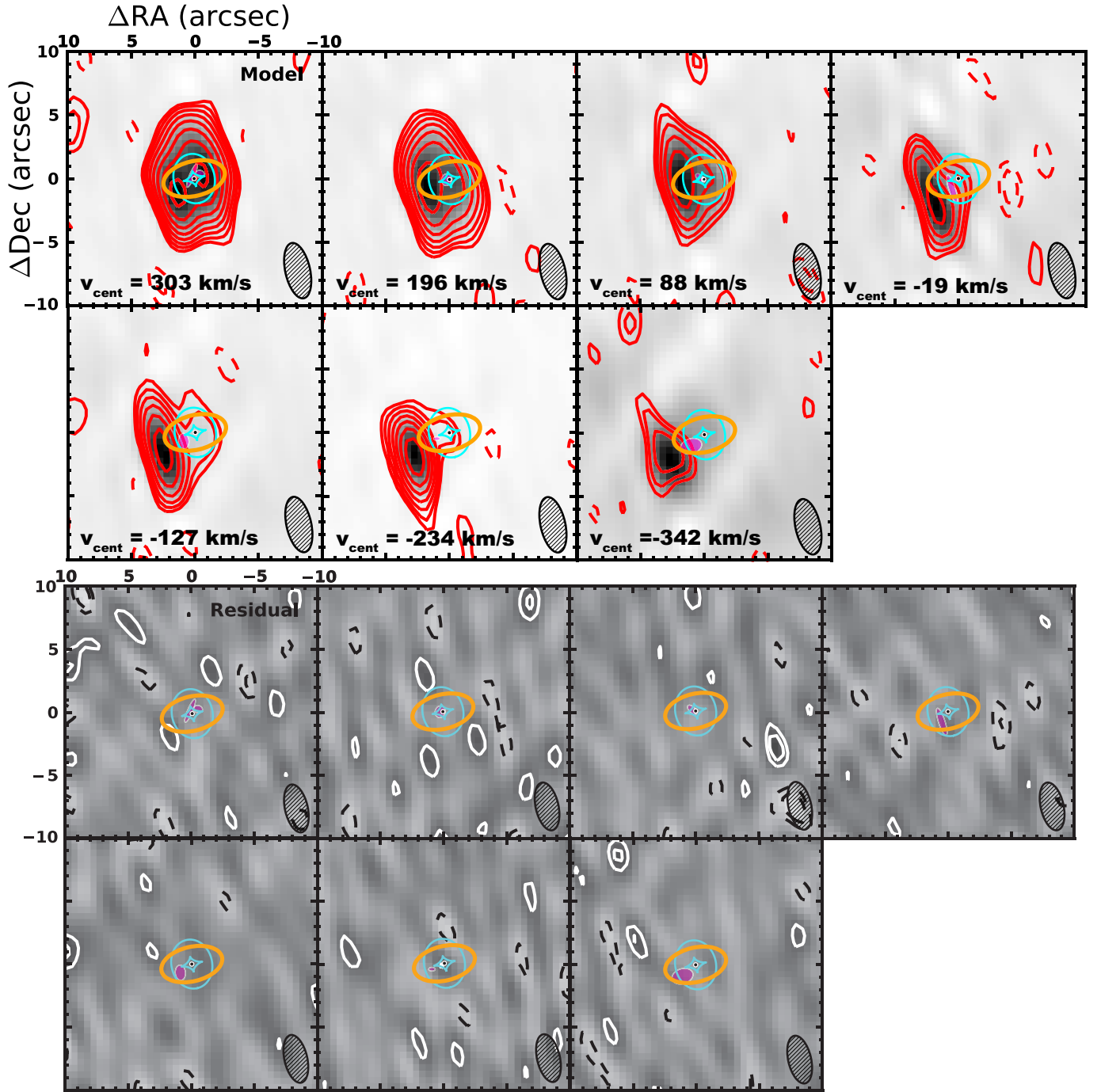


FIG. 6.— Best-fit lens models of the PdBI CO($J=2 \rightarrow 1$) data in different velocity channels, as listed in Table 4. Top: each panel corresponds to a channel map of width 107.5 km s^{-1} of the observed emission (red) overlaid on around the annotated central velocity where the observed emission (red contours) is over-plotted atop the best-fit model (grayscale). Bottom: residual images obtained by taking a Fourier transform after subtracting the best-fit model from the data in the uv -domain. In all panels, the location of the foreground lensing galaxy is indicated by a black dot and its critical curve is traced by the orange solid line; locations and morphologies (half-light radii) of the reconstructed sources are represented by magenta ellipses; the caustic curves are represented as cyan lines. Contours start at $\pm 3\sigma$ and increment at steps of $3 \times 2^n \sigma$, where n is a positive integer. The beam of the PdBI observations is shown in the bottom right corner. The reconstructed source-plane positions, as represented by the magenta ellipses, demonstrate an intrinsic velocity gradient of the CO($J=2 \rightarrow 1$) emission in RXJ1131. The best-fit model of the red-most channel (top left panel) contains two source components — RXJ1131 and its companion galaxy.

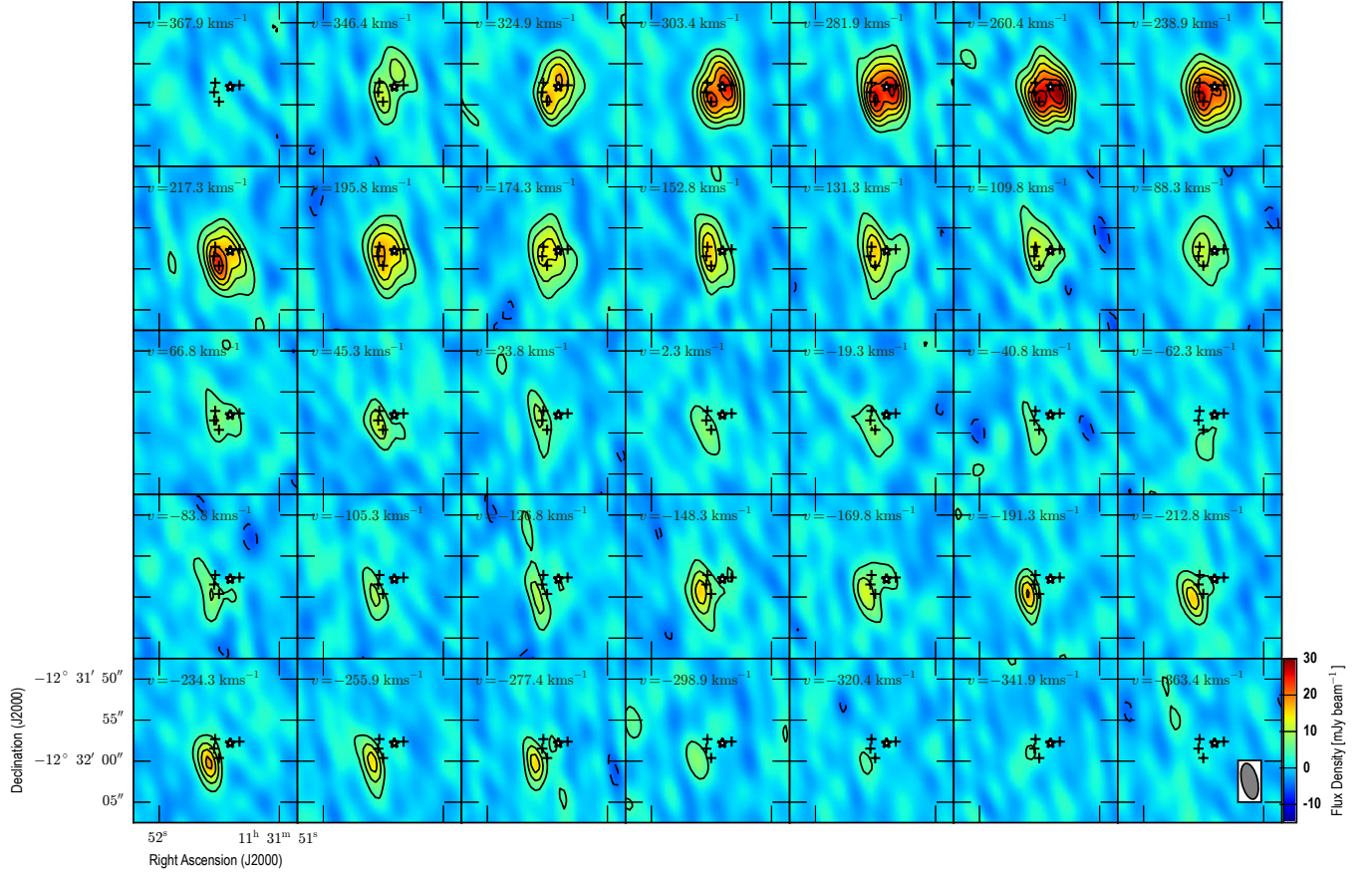


FIG. 7.— Channel maps of the PdBI CO($J=2 \rightarrow 1$) data cube toward RXJ1131 at 21.5 km s^{-1} resolution. Black crosses indicate the positions of the lensed knots (AGN emission, which correspond to components ABCD in C06). The central white-filled star indicates the position of the foreground lensing galaxy (component G in C06). Central velocities are shown at the top of each map. Contours start and increment at steps of $\pm 3\sigma$. The beam is denoted in the bottom right panel.

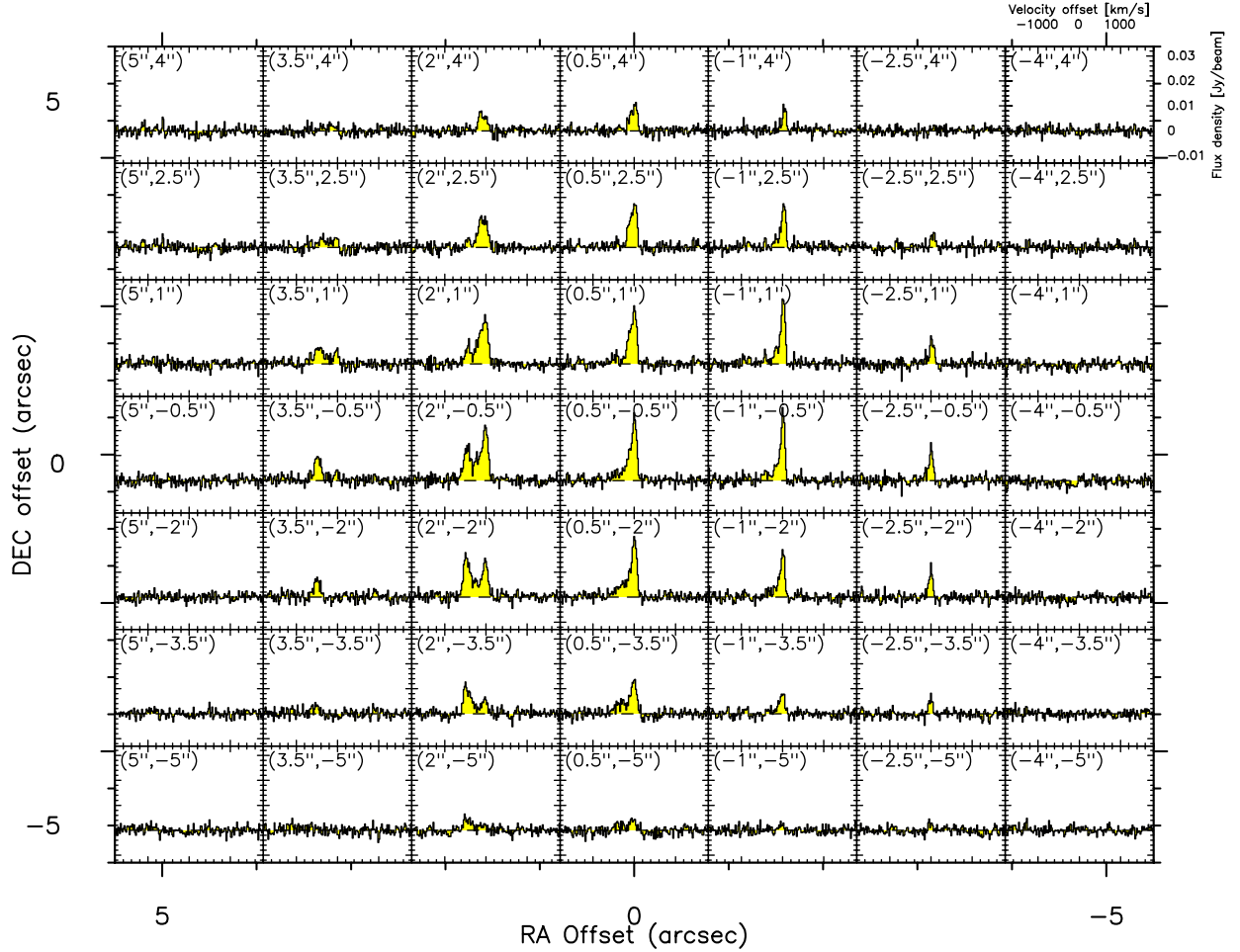


FIG. 8.— CO($J=2 \rightarrow 1$) spectrum as a function of position, binned by 3 pixels in each direction ($1''.5$). The spectra map covers an extent of $\sim 10'' \times 10''$ centered on the pixel that corresponds to coordinates of the lensing galaxy ($\alpha_{J2000} = 11^{\text{h}}31^{\text{m}}51^{\text{s}}.44$, $\delta_{J2000} = -12^{\circ}31'58''.3$). Spatial offset in arcsec is denoted in top left corner of each panel. The velocity and flux density scales are denoted in the top right panel.

of differential lensing, where the redshifted emission is apparently much brighter than the blueshifted component, as indicated by the difference in their magnification factor (μ_L), which varies from 8.7 to 3.1 across the CO($J=2 \rightarrow 1$) line (Table 4). A secondary effect contributing to the asymmetry is caused by the CO emission in the companion in the redshifted velocity channels. The variation in μ_L found across channels is consistent with the source plane positions relative to the caustics in Figure 6, where the red wing emission mainly originates near the cusp of the caustic and the blue wing emission is located beyond the caustics. In fact, the intrinsic line flux of the redshifted and blueshifted emission in RXJ1131 (after subtracting a contribution from the companion) are $I_{\text{CO}(J=2 \rightarrow 1)} = 1.26 \pm 0.23 \text{ Jy km s}^{-1}$ and $1.25 \pm 0.23 \text{ Jy km s}^{-1}$, respectively, implying an intrinsically symmetric line profile (Figure 5). This is consistent with the symmetric source-plane velocity gradient in our lens model (Figure 6 and Figure 9).

4.2. CO($J=2 \rightarrow 1$) Kinematics

Fitting two Gaussians with a common FWHM to the “intrinsic” CO($J=2 \rightarrow 1$) line profile of RXJ1131 (after correcting for lensing using the magnification factors for var-

ious channels and separating the emission from RXJ1131 and its companion), we find a roughly symmetric double-horned profile with a flux ratio of 1.2 ± 0.4 between the peaks, which are separated by $\Delta v_{\text{sep}} = 387 \pm 45 \text{ km s}^{-1}$, and each with a FWHM of $220 \pm 72 \text{ km s}^{-1}$. The peak separation obtained from this “intrinsic” line profile is slightly lower than that obtained from the observed spectrum (i.e., without lensing corrections). This discrepancy is likely a result of differential lensing, which causes the line peak of the red wing to shift towards higher velocity channels, and thereby biasing the centroid of one Gaussian to higher velocity than otherwise. To facilitate a comparison (§5.1.1) with previous works, which were observed at lower spectral resolution, we also fit a single-Gaussian to the intrinsic line profiles. This yields FWHMs of $600 \pm 160 \text{ km s}^{-1}$ for RXJ1131 and $73 \pm 43 \text{ km s}^{-1}$ for the companion galaxy.

A clear velocity gradient and a high velocity dispersion ($\gtrsim 400 \text{ km s}^{-1}$) near the central region are seen in Figure 2. While beam smearing is inevitably the dominant factor in the observed velocity dispersion at the spatial resolution of these data, the exceedingly high velocity dispersion may hint at potential perturbations from the AGN, or internal turbulence due to interactions with the companion,

and/or instability due to the large gas content. Therefore, in this scenario, RXJ1131 is consistent with a disrupted disk galaxy hosting an optically bright quasar and in the process of merging.

4.3. CO($J=2 \rightarrow 1$) Dynamical Modeling

As discussed in §4.1.1, we interpret RXJ1131 as a disk galaxy given its reconstructed source-plane locations of various kinematic components displaying a velocity gradient with a symmetric double-horned line profile (Figure 5, Figure 6 and, left panel of Figure 9), and the disk-like morphology found for source-plane reconstructed optical-NIR emission (C06). Assuming the velocities of the respective channels used in the lens modeling correspond to solely the tangential component of the true velocity vector of a rotating disk (i.e., along the major axis), we extract a one dimensional PV diagram in Figure 9 by slicing across their source plane positions along this major axis (PA: 121°).

We then attempt to characterize the molecular gas kinematics using an empirically-motivated disk model (e.g., Courteau 1997; Puech et al. 2008; Miller et al. 2011):

$$V = V_0 + \frac{2}{\pi} V_a \arctan\left(\frac{R}{R_t}\right), \quad (1)$$

where V is the observed velocity, V_0 is the velocity at dynamical center, V_a is the asymptotic velocity, and R_t is the “turnover” radius at which the rising part of the curve begins to flatten. We perform non-linear least squares fitting using an orthogonal distance regression to find the best-fit parameters, taking into account the uncertainties in both velocity (channel width) and distance offset. We also place an upper limit on $R_t < 15$ kpc to keep this parameter physical (e.g., Puech et al. 2008; Miller et al. 2011). The parameter uncertainties are inferred based on a Monte Carlo simulation of 500 iterations, where the input parameters are perturbed according to random Gaussian distributions with standard deviations corresponding to their uncertainties. Using this model, we find $V_a = 975 \pm 387 \text{ km s}^{-1}$, $R_t = 10.7 \pm 5.7 \text{ kpc}$, and $V_0 = 28 \pm 40 \text{ km s}^{-1}$. $V_a = 988 \pm 618 \text{ km s}^{-1}$, $R_t = 10.9 \pm 7.8 \text{ kpc}$, and $V_0 = 0 \pm 9 \text{ km s}^{-1}$. However, since the emission is not resolved along the flat regime of the rotation curve, the asymptotic velocity and the “turnover” radius are poorly constrained. In particular, V_a and R_t are highly correlated with a Pearson coefficient $R = 0.998$, and -0.400 between V_a and V_0 .

The asymptotic velocity (V_a) — an extrapolation of the model out to radius beyond the disk scale-length and half-light radius — is not equivalent to the maximum observed velocity (V_{max}), which is commonly used in literature to parameterize disk rotation. The arctangent model is most commonly used in studies of the Tully-Fisher relation, where an extrapolation to $V_{2.2}$ (velocity at 2.2 disk scale-length or ~ 1.375 half-light radius, or $\sim 0.7R_{\text{opt}}$ ⁴) is typically adopted as the rotation velocity (V_{max} in their terminology), since this corresponds to the radius at which

the velocity of a pure exponential disk peaks (Courteau & Rix 1997). Here, we adopt the maximum observed velocity $V_{\text{rot}} = 345 \pm 303 \pm 55 \text{ km s}^{-1}$ at 6 ± 3 kpc from the dynamical center as a proxy to the rotation velocity. This radius corresponds to $\sim 0.6 R_e$, where R_e is the half-light radius ~ 10.3 kpc inferred from the *HST* *I*-band lens model (C06; converted to our cosmology). We note that the source plane half-light radius varies substantially with wavelength. In particular, the half-light radius is found to be ~ 4 kpc and ~ 7 kpc in *V*-band (B08) and *H*-band (C06), respectively. The CO gas is thus of similar spatial extent as in the *H* and *I*-bands.

In the rest-frame, emission in the observed-frame *H*-band corresponds to NIR emission ($\sim 1 \mu\text{m}$), tracing radiation from the accretion disk surrounding the central AGN and also from old and evolved stellar populations; *I*-band corresponds to roughly the optical *V*-band, tracing stellar radiation from existing, less massive (i.e., longer-lasting) stars; *V*-band corresponds to roughly *U*-band, tracing radiation from massive young stars in the host galaxy. Hence, the relative compactness observed in the *V*-band may be explained in part due to the fact that the emission in this band is more susceptible to dust extinction than in other bands and/or dominated by a central starburst caused by higher concentrations of star-forming gas towards the central regions — owing to gravitational perturbations induced from interactions with the companion (e.g., Di Matteo et al. 2005). This would be consistent with the picture that old stars form first and constitute the bulge component of a spiral galaxy, and that nuclear starbursts (in the inner few kpc) can be triggered at a later time as the progenitor disk galaxy interacts with other galaxies to form a larger bulge.

4.4. Dynamical Mass

Assuming the gas to be virialized, the dynamical mass can be approximated by $M_{\text{dyn}} \sim \sigma^2 R / G$, where σ is the velocity dispersion, or the rotational velocity in the case of a rotating disk model (i.e., $\sigma = V_{\text{rot}} \sin i$). Using a rotational velocity $V_{\text{rot}} \sin i = 345 \pm 303 \text{ km s}^{-1}$ (see §4.3), we find a dynamical mass of $M_{\text{dyn}} \sin^2 i (< 6 \text{ kpc}) = 1.7 \pm 1.3 \times 10^{11} M_\odot$ enclosed within the CO-emitting region in RXJ1131. If we instead consider the CO($J=2 \rightarrow 1$) line peak separation ($\Delta v_{\text{sep}}/2 \sim 200 \text{ km s}^{-1}$) as the rotation velocity, we find $M_{\text{dyn}} \sin^2 i (< 6 \text{ kpc}) = 5.8 \times 10^{10} M_\odot$. We derive an inclination angle of 56.4° from the morphological axial ratio of $a/b \sim 1''.8/3''.25$, which we estimate from the source-plane image reconstructed by C06 (Figure 3 in their paper). This corresponds to an inclination-corrected dynamical mass of $8.3 \times 10^{10} M_\odot < M_{\text{dyn}} < 25 \times 10^{10} M_\odot$. Our estimate should be considered at best an upper limit since the gas in RXJ1131 is unlikely virialized. In the following sections, we use the lower limit $(8.3 \pm 1.9) \times 10^{10} M_\odot$ as the dynamical mass as it is derived in a manner similar to what is commonly used in literature (e.g., Solomon et al. 1997, hereafter S97; Downes & Solomon 1998, hereafter DS98; Greve et al. 2005, hereafter G05).

Using the velocity dispersion ($\sigma = 30 \text{ km s}^{-1}$) obtained by fitting a single Gaussian to the de-lensed

⁴ Radius enclosing 83% of the light distribution.

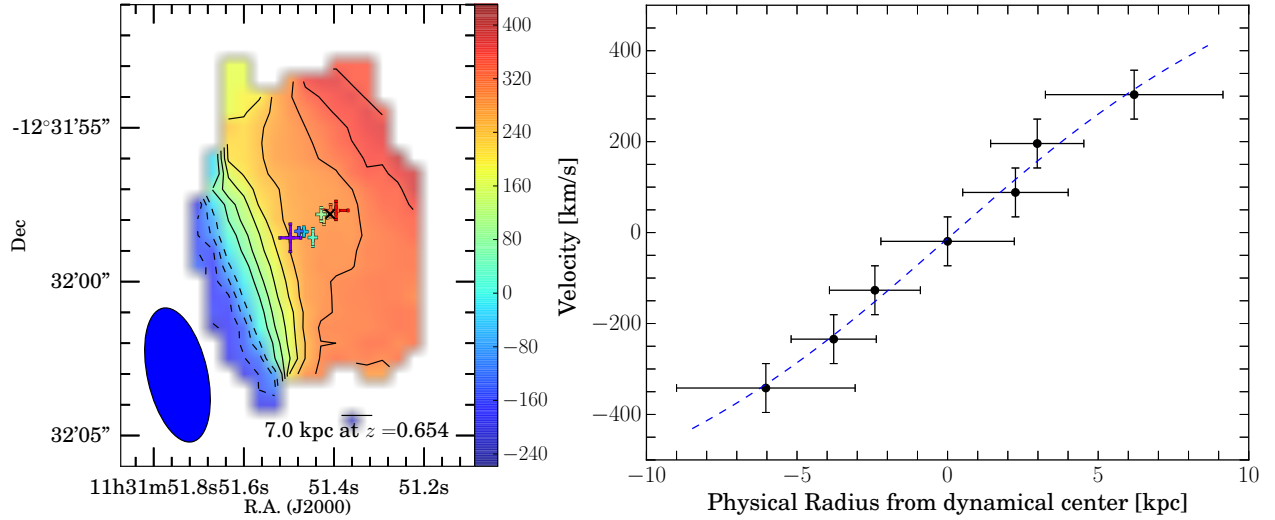


FIG. 9.— Left: Source-plane positions from best-fit CO($J=2 \rightarrow 1$) lens models are indicated with their associated uncertainties atop the observed first-moment map. Source-plane positions obtained from the best-fit lens models (presented in §4.1) are shown as markers color-coded by their velocities atop the observed first moment map (i.e., in the image-plane; see Figure 2). The contours are at steps of 50 km s^{-1} . Despite the distorted first moment map in the image-plane due to differential lensing and beam smearing effects, the source-plane velocity gradient reconstructed from dynamical lens modeling suggests that RXJ1131 is intrinsically a kinematically-ordered disk. Right: PV slice extracted along the fitted major axis at $\text{PA} = 121^\circ$ based on the reconstructed source-plane velocity gradient. Dashed line shows the best-fit “rotation curve” using an arctangent model. The vertical error bars show the channel width for each model and the horizontal error bars are the 1σ uncertainties on the source-plane positions along the major axis.

line profile of the companion and a half-light radius of $R_{\text{CO}} = 4.2 \pm 2.8 \text{ kpc}$ from the best-fit lens model, we find a dynamical mass of $M_{\text{dyn}} = (3.5 \pm 2.3) \times 10^9 M_\odot$ for the companion, assuming an inclination angle of $i = 30^\circ$. The uncertainty here only includes that of the CO source size. On the other hand, we find $M_{\text{dyn}} \sin^2 30^\circ = 5.8 \times 10^8 M_\odot$ if we adopt the better-constrained V-band source size of $\sim 700 \text{ pc}$ (B08). Since the V-band based dynamical mass measurement is substantially lower than the gas mass, the V-band emitting region may appear to be much smaller than its true extent due to dust obscuration.

The CO-based dynamical mass estimates correspond to a mass ratio of $\sim 24:1$ between RXJ1131 and the companion, with a gas mass ratio of $\sim 7:1$ derived in §4.1.1. We thus classify the system as a *gas-rich, “wet” minor merger*.

4.5. SED Modeling

We fit dust SED models to the $24 \mu\text{m}$ – 2.2 mm photometry using a modified-blackbody (MBB) function with a power-law attached to the Wien side to account for the MIR excess due to emission of warm and small dust grains. The IRAS $60 \mu\text{m}$ and $100 \mu\text{m}$ upper limits are included to constrain the dust peak and an uncertainty from absolute flux calibration of $\sim 15\%$ is added in quadrature for the PdBI 2 mm continuum in our fitting procedure. Here, we use a flux density of $S_{2\text{mm}} = 0.27 \text{ mJy}$ derived in §3.3 instead of the deblended 0.39 mJy listed in Table 2 to exclude synchrotron emission (see §3.3) in dust SED modeling.

The fit is performed using the code MBB_EMCEE (e.g., Riechers et al. 2013; Dowell et al. 2014), which samples the posterior distributions using an MCMC approach and uses instrumental response curves to perform color correction. The model is described by five free parameters: the rest-frame characteristic dust temperature (T_d), the emis-

TABLE 5
SED FITTING RESULTS

Parameters		With $24 \mu\text{m}$	Without $24 \mu\text{m}$
T_d	(K)	54^{+8}_{-10}	55^{+21}_{-20}
β		$1.6^{+0.5}_{-0.4}$	$2.2^{+0.3}_{-0.3}$
α		$1.6^{+0.5}_{-0.6}$	$8.5^{+7.0}_{-6.2}$
λ_0^a	(μm)	559^{+278}_{-324}	365^{+111}_{-120}
λ_{peak}^b	(μm)	159^{+19}_{-40}	155^{+38}_{-43}
$f_{\text{norm}, 500 \mu\text{m}}^c$	(mJy)	55^{+13}_{-13}	59^{+6}_{-6}
L_{FIR}^d	($10^{12} L_\odot$)	$3.81^{+1.92}_{-1.97}$	$4.24^{+2.17}_{-2.00}$
M_d^e	($10^8 M_\odot$)	16^{+5}_{-12}	14^{+5}_{-7}

NOTE. — Errors reported here are $\pm 1\sigma$. L_{FIR} and M_d are not corrected for lensing.

^a Observed-frame wavelength where $\tau_\nu = 1$

^b Observed-frame wavelength of the SED peak

^c Observed-frame flux density at $500 \mu\text{m}$

^d Rest-frame 42.5 – $122.5 \mu\text{m}$ luminosity

^e Derived assuming an absorption mass coefficient of $\kappa = 2.64 \text{ m}^2 \text{ kg}^{-1}$ at $\lambda = 125.0 \mu\text{m}$ (Dunne et al. 2003)

sivity index (β), the power-law index (α), the flux normalization at $500 \mu\text{m}$ (f_{norm}), and the observed-frame wavelength at which the emission becomes optically thick (λ_0). We impose a uniform prior with an upper limit of 100 K on T_d (see e.g., Sajina et al. 2012), a Gaussian prior centered around 1.9 with a standard deviation of 0.3 on β , and a uniform prior with an upper limit of $1000 \mu\text{m}$ on λ_0 . We check for chain convergence by requiring that the autocorrelation length of each parameter is less than the number of steps taken for the burn-in phase (which are then discarded). Here we report the statistical means and the 68% confidence intervals in the marginal PDFs as the best-fit parameters, as listed in Table 5. The best-fit models are shown in Figure 10 along with the broadband photometry that is listed in Table 2.

In the first model, we attempt to constrain the power-law index by including the $24\ \mu\text{m}$ data. Based on the resulting posterior PDFs, we find an apparent **IR luminosity (rest-frame $8-1000\ \mu\text{m}$) of $8.22^{+2.75}_{-2.98} \times 10^{12} L_{\odot}$, a far-IR luminosity (rest-frame $42.5-122.5\ \mu\text{m}$) of $3.81^{+2.04}_{-1.92} \times 10^{12} L_{\odot}$, **$3.81^{+1.92}_{-1.97} \times 10^{12} L_{\odot}$** , and a dust mass of $16^{+5}_{-12} \times 10^8 M_{\odot}$, **all of which are** uncorrected for lensing **magnification**. For the mass absorption coefficient, we adopt $\kappa = 2.64\ \text{m}^2\text{kg}^{-1}$ at rest-frame $125.0\ \mu\text{m}$ (Dunne et al. 2003). The dust mass uncertainty does not include that of the absorption coefficient.**

A fit including the MIR $24\ \mu\text{m}$ photometry is likely an upper limit on the far-IR luminosity due solely to star formation in the AGN host galaxy. If we instead fit for a model excluding this constraint, two major consequences are immediately apparent. First, the power-law index is poorly-constrained (see Table 5). Second, the steep power-law implies only a small contribution from the power-law regime to the total IR luminosity as compared to the graybody component. Thus, the far-IR luminosity in this model should, in principle, correspond to a lower limit on the cold dust emission. Using the best-fit parameters for this model, we find a total IR luminosity L_{IR} (rest-frame $8-1000\ \mu\text{m}$) of $9.71^{+6.14}_{-6.05} \times 10^{12} L_{\odot}$, **$8.67^{+5.27}_{-5.27} \times 10^{12} L_{\odot}$** , a far-IR luminosity L_{FIR} of $4.72^{+2.54}_{-2.26} \times 10^{12} L_{\odot}$, **$4.24^{+2.17}_{-2.00} \times 10^{12} L_{\odot}$** and a dust mass M_{dust} of $11^{+5}_{-6} \times 10^8 M_{\odot}$, **$14^{+5}_{-7} \times 10^8 M_{\odot}$** , all of which are uncorrected for lensing. Taken at face value, this implies an FIR-to-IR luminosity ratio of $\sim 58 \pm 35\%$ **$\sim 49 \pm 38\%$** .

The dust temperature from both models is similar to that of ULIRGs at $0.6 < z < 1.0$ ($54 \pm 5\ \text{K}$; Combes et al. 2013, hereafter C13). The far-IR luminosity is comparable in both models, which is not surprising given the lack of constraints in the MIR. For the subsequent analysis, we adopt the physical quantities from the first model (i.e., with constraints at $24\ \mu\text{m}$). The choice of SED model does not affect the derived star formation rate (SFR) given the similar far-IR luminosity. ~~Yet, the dust mass is higher by a factor of ~ 2 in the former but consistent within the uncertainties,~~ and their dust masses are consistent within the uncertainties. We correct for lensing using the median magnification factor ($\mu_L = 5.5$) from the CO lens models. This yields a L_{FIR} of $(6.9 \pm 3.6) \times 10^{11} L_{\odot}$ and an intrinsic total IR luminosity of $\sim 1.5 \times 10^{12} (5.5/\mu_L) L_{\odot}$, implying that RXJ1131 can be classified as an ULIRG. Assuming a Salpeter (1955) initial mass function (IMF), we find a SFR_{FIR} of $120 \pm 63 M_{\odot}\ \text{yr}^{-1}$ using a standard conversion (Kennicutt 1998).

We derive the stellar mass of RXJ1131 by fitting SED models to the rest-frame UV-to-mm photometry using the high- z version of the MAGPHYS code (da Cunha et al. 2008, 2015). Two sets of stellar templates modeled using either the Bruzual & Charlot (2003) or the unpublished Charlot & Bruzual 2007 stellar population synthesis code are provided in the MAGPHYS package. We adopt the former set. To minimize contaminations from the quasar, we only fit to the *HST*, *Herschel*, and PdBI data, where both

the *HST* and the PdBI 2 mm photometry are de-blended from the AGN (see bottom section of Table 2). The input photometry are corrected for lensing using their respective magnification factors to account for differential lensing (light blue circles in Figure 10). We thus find a stellar mass of $M_* = 2.95^{+1.32}_{-0.86} \times 10^{10} M_{\odot}$, which is the median value of the posterior probability distribution and the uncertainties are derived from the 16th and 84th percentiles. We note that the models are over-fitted with a best-fit $\chi^2 = 0.41$ which is unsurprising due to sparse sampling of the SED compare to the number of free parameters. The resulting dust mass and IR luminosity are consistent with those obtained from the MBB+power-law models within the uncertainties, albeit some differences in the assumptions behind the two methods. The consistency may be attributed to the large uncertainties arising from the lack of photometric constraints on the models and the fact that the best-fit parameters from the MBB method are similar to those of the MAGPHYS method.

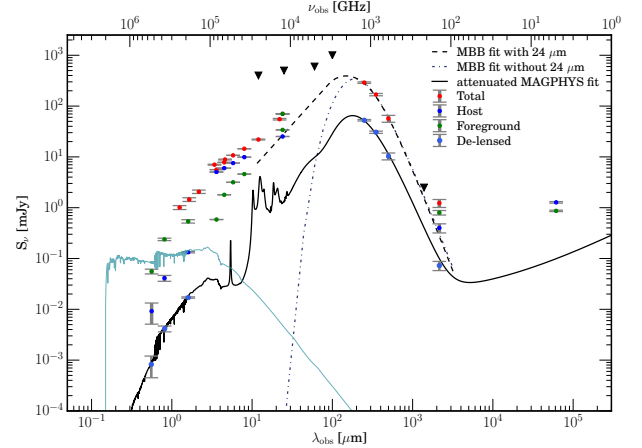


FIG. 10.— SEDs of RXJ1131 at $z_{\text{CO}}=0.654$ and the lensing galaxy at $z=0.295$. The photometry data (colored markers) are listed in Table 2, except for those shown in light blue circles, which are corrected for lensing magnification (see §4.5). Assuming an MBB+power-law model for the thermal dust emission towards RXJ1131, the dashed (dashed-dotted) line corresponds to the best-fit model with (without) MIR constraint at $24\ \mu\text{m}$. The solid black line shows the best-fit SED model with dust attenuation (light blue solid line) obtained using the MAGPHYS code, **obtained using the MAGPHYS code, whereas the light blue solid line shows the unattenuated stellar emission.**

5. DISCUSSION

The properties of RXJ1131 and the companion derived in this section are summarized in Table 6.

5.1. ISM Properties

In this section, we derive the gas properties of the merging system RXJ1131 based on $\text{CO}(J=2 \rightarrow 1)$ and compare them with those reported by C13⁵ — the largest sample of CO-detected ULIRGs at similar redshift

⁵ The far-IR luminosity in C13 is derived based on $60\ \mu\text{m}$ and $100\ \mu\text{m}$ IRAS fluxes, and using a different definition of L_{FIR} : rest-frame $40-500\ \mu\text{m}$. Following this convention, we find a far-IR luminosity of $L_{\text{FIR}} = (8.8 \pm 0.4) \times 10^{11} (\mu_L/5.5)^{-1} L_{\odot}$ and a SFR of $(150 \pm 70) M_{\odot}\ \text{yr}^{-1}$ for RXJ1131.

TABLE 6
PHYSICAL PROPERTIES OF RXJ1131 AND ITS
COMPANION

Parameter	Unit	Value
r_{32}		0.78 ± 0.62
$\text{FWHM}_{\text{CO}(2-1), \text{RXJ1131}}$ ^a	km s^{-1}	220 ± 72
$\text{FWHM}_{\text{CO}(2-1), \text{RXJ1131}}$ ^b	km s^{-1}	600 ± 160
$\text{FWHM}_{\text{CO}(2-1), \text{companion}}$ ^b	km s^{-1}	73 ± 43
$M_{\text{gas, RXJ1131}}$	$10^{10} M_{\odot}$	1.38 ± 0.33
$M_{\text{gas, companion}}$	$10^9 M_{\odot}$	1.92 ± 0.09
$R_{\text{CO, RXJ1131}}$	kpc	6.2 ± 3.0
$R_{\text{CO, companion}}$	kpc	4.2 ± 2.8
$M_{\text{dyn, RXJ1131}}$	$10^{10} M_{\odot}$	8.3 ± 1.9 ^c
$M_{\text{dyn, companion}}$	$10^9 M_{\odot}$	3.5 ± 2.3 ^c
f_{gas}	%	18 ± 4 ^d
f_{mol}	%	34 ± 16
L_{IR}	$10^{12} L_{\odot}$	~ 1.5
L_{FIR}	$10^{11} L_{\odot}$	6.9 ± 3.6
SFR_{FIR}	$M_{\odot} \text{ yr}^{-1}$	120 ± 63
M_{dust}	$10^8 M_{\odot}$	~ 3
GDR		54 ± 13
τ_{depl}	Myr	102 ± 25
M_{*}	$10^{10} M_{\odot}$	3.0 ± 1.0
M_{BH} ^e	$10^7 M_{\odot}$	~ 8
$M_{\text{BH}}/M_{\text{bulge}}$	%	$>0.27^{+0.11}_{-0.08}$

NOTE. — All the parameters have been corrected for lensing magnification. The physical parameters are derived for RXJ1131 and the companion as a single system unless otherwise stated.

^a From fitting a double Gaussian with a common FWHM to the de-lensed spectrum.

^b From fitting a single Gaussian to the de-lensed spectrum.

^c Excluding systematic uncertainties.

^d Excluding uncertainties in the dynamical masses.

^e Sluse et al. (2012).

($0.6 < z < 1.0$). Their results are based on spatially unresolved CO($J=2 \rightarrow 1$) and CO($J=4 \rightarrow 3$) line observations with the IRAM 30-m single-dish telescope.

5.1.1.1. Linewidths and Sizes

The FWHM linewidth of $\Delta v \sim 600 \pm 160 \text{ km s}^{-1}$ found for RXJ1131 by fitting a single Gaussian is considerably larger than the statistical average in the C13 sample (370 km s^{-1}) and local ULIRGs (median: $300 \pm 85 \text{ km s}^{-1}$, with the largest being 480 km s^{-1} ; S97). Linewidths exceeding 500 km s^{-1} are also commonly observed in high- z starburst galaxies (e.g., G05) and high- z quasar host galaxies (e.g., Coppin et al. 2008), which are believed to originate from mergers. The wider CO linewidth observed in RXJ1131 also supports a merger picture.

The CO gas in RXJ1131 is $\sim 6 \pm 3 \text{ kpc}$ in radius (in the source plane), which is more extended than the average of $3.5 \pm 2.3 \text{ kpc}$ in a sample of disk-like U/LIRGs studied by Ueda et al. (2014), but consistent with their range of $1.1\text{--}9.3 \text{ kpc}$. Our CO size is also consistent with that of high- z ($z > 1$) galaxies ($R \sim 4\text{--}20 \text{ kpc}$; G05; Daddi et al. 2010; Riechers et al. 2011; Ivison et al. 2011) and local U/LIRGs in the Gao & Solomon (1999) sample ($R \lesssim 10 \text{ kpc}$).

5.1.2. Gas Mass Fractions and Gas-to-dust Ratio

We find a dynamical gas mass fraction of $f_{\text{gas}} = M_{\text{gas}}/M_{\text{dyn}} = 19 \pm 5\%$ **$18 \pm 4\%$** and a baryonic gas mass fraction of $f_{\text{mol}} = M_{\text{gas}}/(M_{\text{gas}} + M_{*}) = 32^{+7}_{-12}\%$ **for RXJ1131 $34 \pm 16\%$ for the merger system (i.e., RXJ1131 and companion)**. Recent studies find that the baryonic gas fraction of starburst galaxies has decreased from $f_{\text{mol}} \sim 40\%$ to $\lesssim 10\%$ between $z \sim 2$ and $z \sim 0$ (S97; Gao & Solomon 2004; Tacconi et al. 2006), and from $f_{\text{mol}} \sim 50\%$ to $\sim 5\%$ between the same redshift range for “normal star-forming” galaxies (Geach et al. 2011; Saintonge et al. 2011; Tacconi et al. 2013)⁶. Both the dynamical and baryonic gas mass fractions of RXJ1131+companion are thus consistent with the trend of decreasing molecular gas content since $z \sim 2$ which has been suggested as the cause for the decline in sSFR and cosmic star formation history towards $z \sim 0$ (e.g., Tacconi et al. 2013; Carilli & Walter 2013; Genzel et al. 2015).

Using the lensing-corrected dust mass, we find a galactic-scale gas-to-dust ratio (GDR) of 40 ± 34 **54 ± 13** . ~~This would be higher by a factor of two if we were to adopt a dust mass from the other SED fit that is unconstrained at $24 \mu\text{m}$.~~ This GDR is lower than the statistical average of 206 in the C13 sample but is well within the broad range of values measured over their entire sample ($\sim 1\text{--}770$). Our ratio is also consistent with high- z SMGs (Bothwell et al. 2013) and local ULIRGs (Wilson et al. 2008), but lower than that of the Milky Way by $\sim 47\sigma$ (ignoring systematic uncertainties; Li & Draine 2001; Zubko et al. 2004; Draine et al. 2007).

There are a number of systematic uncertainties associated with the derived gas-to-dust ratio, in particular the mass opacity coefficient κ , the α_{CO} conversion factor, and the brightness temperature ratio r_{21} . If we instead use the “Galactic” α_{CO} value, which may be more appropriate for some ULIRGs (e.g., Papadopoulos et al. 2012) and minor mergers (Narayanan et al. 2012), the gas mass (and thus gas-to-dust ratio) would be ~ 6 times higher. We note that this gas mass is physically possible based on the dynamical mass constraints derived in §4.4. On the other hand, we would also obtain a higher gas mass if we assumed sub-thermal excitation between CO($J=2 \rightarrow 1$) and CO($J=1 \rightarrow 0$) emission. We also note that the gas-to-dust ratio derived for RXJ1131 may be biased low as the gas is likely to be more extended than the optically thick dust. Consequently, the overall magnification factor for the CO gas may be lower than the optically thick dust, which dominates the far-IR luminosity. This would lead to an overestimation of the dust mass by adopting the CO magnification factor for the dust.

5.1.3. Star Formation Efficiency and specific SFR

To first order, the star formation efficiency ($\text{SFE} = L_{\text{FIR}}/M_{\text{gas}}$) indicates the star formation rate per unit solar mass of molecular gas available in a galaxy. Using a wavelength range of $40\text{--}500 \mu\text{m}$ defined in C13 for the far-IR luminosity, we find an SFE of $58 \pm 10 L_{\odot} M_{\odot}^{-1}$, which

⁶ These authors use the “Galactic” value of $\alpha_{\text{CO}} = 4.6 M_{\odot} (\text{K km pc}^2)^{-1}$ to compute the molecular gas mass.

is on the low end among other U/LIRGs at $z < 0.6$ (S97; Combes et al. 2011) but consistent with those of low- z spiral galaxies ($z < 0.1$; SV05) and high- z disk-like galaxies, which are also IR luminous galaxies with $L_{\text{IR}} \sim 10^{12} M_{\odot}$ (Daddi et al. 2008, 2010). This suggests that the merger system is converting gas into stars at an efficiency similar to those of “normal” star-forming disk-like galaxies rather than starburst galaxies (Tacconi et al. 2008; Riechers et al. 2011, C13). This is in agreement with its disk-like kinematic signatures and its extended molecular gas distribution. Assuming the star formation continues at the current rate without gas replenishment, the SFE corresponds to a gas depletion time of $\tau = 102 \pm 25$ Myr.

The specific star formation rate ($\text{sSFR} = \text{SFR}/M_{*}$) of $4_{-2.4}^{+2.6} \text{ Gyr}^{-1}$ derived for RXJ1131 is $\lesssim 1.5\sigma$ above the main sequence according to the redshift-dependent “main sequence” relation in Tacconi et al. (2013, and references therein). Given that RXJ1131 share similar star formation rate, star formation efficiency, and CO disk size as other “main sequence” disk galaxies, the small elevation in sSFR over the main sequence at $z \sim 0.7$ suggests that the star formation activity in RXJ1131 may be enhanced by interactions with the companion.

Given that the host galaxy of RXJ1131 is an extended disk with low star formation efficiency in a minor merger system, the removal of angular momentum of the gas via gravitational torque is likely inefficient to convert the entire gas disk into a massive stellar bulge. Hence, the disk component may be retained upon merging with the companion. This scenario is consistent with the results from recent simulations, which suggest that bulge formation maybe suppressed in gas-rich mergers, thereby allowing the formation of large disk galaxies with low bulge-to-disk ratios (Springel & Hernquist 2005; Robertson et al. 2006; Hopkins et al. 2009). This also supports the idea that not all mergers will transform into elliptical galaxies, as in the classical picture (Toomre & Toomre 1972).

5.2. Systemic Redshift and Velocity Offset

Sluse et al. (2007) report two sets of AGN lines observed in RXJ1131. The first set of lines is at $z \sim 0.653$ **0.654**, including the narrow component of the Balmer lines, the [O III] 4959, 5007 Å lines, and the Mg II 2798 Å absorption line; the second set is at $z \sim 0.658$, including the broad component of the Balmer lines and the Mg II 2798 Å emission line. Using the CO line center redshift as the ~~systematic~~ **systemic** redshift, we find that the redshift of the first set is fully consistent with the systemic redshift. This supports previous claims that [O III] lines, tracing the narrow line region (NLR), are good proxies to the true systemic redshift (e.g., Vrtilek 1985; Nelson 2000). ~~On the other hand, the second set of lines is blueshifted by $\sim 780 \text{ km s}^{-1}$, indicating that the broad line region (BLR) of the AGN is dynamically offset from the centroid of its host galaxy.~~ **On the other hand, the second set of lines is redshifted by $\sim 715 \text{ km s}^{-1}$.**

~~One explanation for the offset may arise from the fact that BLRs are gravitationally bound to the central AGN, whereas this condition is not necessary for NLRs. From~~

an SDSS sample of > 3800 quasars, Richards et al. (2002) find a median of 97 km s^{-1} and a dispersion of 269 km s^{-1} in the distribution of the offset between [Mg II] and [O III] lines, suggesting that large offsets are uncommon. Nevertheless, offsets as large as $\sim 500 \text{ km s}^{-1}$ have been observed in some cases.

~~Alternatively, large velocity offsets between emission lines of the BLR and the NLR may arise in a recoiling black hole (BH), where its BLR is moving at high velocity relative to the bulk of its host galaxy (Madau & Quataert 2004; Bonning et al. 2007; Loeb 2007). A recoiling black hole is expected when a pair of uneven mass BH coalesce, during which their orbital energy is being released as gravitational wave and a non-zero net angular momentum is being carried away. Depending on their initial conditions, numerical relativity simulations have shown that the recoil velocity can reach up to $\sim 4000 \text{ km s}^{-1}$ for spinning BHs (e.g., Campanelli et al. 2007). Several sources have been proposed as recoiling BH candidates, such as CID 42 at $z = 0.359$ (Civano et al. 2010) and SDSS J0956+5127 at $z \sim 0.714$ (Steinhardt et al. 2012). One notable system is SDSS J0927+2943 at $z \sim 0.713$, where a set of redshifted narrow lines and a second set of blueshifted broad AGN lines have been observed (Komossa et al. 2008), similar to the case for RXJ1131. However, this scenario was recently refuted by Decarli et al. (2014), who confirm that the BLR lines in SDSS J0927+2943 are consistent with the CO systemic redshift. This is in contrast with RXJ1131, where our CO observations confirm the blueshifted BLR. Since this model requires a merged BH, it would imply that RXJ1131 might have been in a previous merger, which would also explain the highly spinning BH in RXJ1131 ($a \sim 0.9$; Reis et al. 2014).~~

5.3. The $M_{\text{BH}}-M_{\text{bulge}}$ Relation

We find a $M_{\text{BH}}/M_{\text{bulge}}$ ratio of $> 0.27_{-8}^{+11} \%$ **$> 0.27_{-0.08}^{+0.11} \%$** using the black hole mass of $M_{\text{BH}} \sim 8 \times 10^7 M_{\odot}$ (Sluse et al. 2012) and the stellar mass derived in §4.5 as an upper limit to the bulge mass. This ratio is consistent with those of other intermediate- z radio-loud AGNs (McLure et al. 2006) but is higher than those of nearby AGNs (Häring & Rix 2004), supporting the emerging picture that quasars grow faster and/or earlier than their host galaxies at higher redshifts (e.g., Walter et al. 2004; Peng et al. 2006; McLure et al. 2006; Riechers et al. 2008). The elevated $M_{\text{BH}}/M_{\text{bulge}}$ ratio of RXJ1131 compared to local AGNs suggests that the bulk of the black hole mass of RXJ1131 is largely in place while its stellar bulge is still assembling.

6. SUMMARY AND CONCLUSIONS

We present PdBI CO($J=2 \rightarrow 1$) and CARMA CO($J=3 \rightarrow 2$) observations towards the quadruply-imaged quasar RXJ1131 at $z_{\text{CO}} \sim 0.654$, making this the first resolved CO study at intermediate redshift. Using the CO line intensities, we find a brightness temperature ratio of $r_{32} = 0.66 \pm 0.41$ between the CO($J=2 \rightarrow 1$) and CO($J=3 \rightarrow 2$) lines, consistent with thermalized exci-

tation but also with the lower excitation seen in normal star-forming disks. We also detect marginally resolved 2 mm continuum emission underlying the CO($J=2 \rightarrow 1$) line and resolved radio continuum emission at 5 GHz in archival VLA data in both the foreground lensing galaxy and RXJ1131.

Based on our lens modeling analysis of different CO($J=2 \rightarrow 1$) velocity channels, we find a secondary CO-emitting source near RXJ1131 whose coordinates are consistent with those of an optically faint companion reported in previous optical studies (C06; B08). The magnification factor inferred for the CO emission in RXJ1131 is found to vary from $\mu_L \sim 3$ to ~ 9 across channels. This is indicative of an extended molecular gas distribution in the host galaxy of RXJ1131, where the different kinematic components of the gas are magnified inhomogeneously, similar to what was found for the $z > 4$ quasar PSS J2322+1944 (Riechers et al. 2008). Upon correcting for lensing magnification and subtracting a contribution from the companion, we find an intrinsically symmetric double-horned CO($J=2 \rightarrow 1$) line profile for RXJ1131. This together with a symmetric source-plane velocity gradient argues for a rotating disk in RXJ1131, in good agreement with previous findings (C06). We find a lensing-corrected gas mass of $M_{\text{gas}} = (1.38 \pm 0.33) \times 10^{10} M_\odot$ for RXJ1131 and $(1.92 \pm 0.09) \times 10^9 M_\odot$ for the companion, corresponding to a gas mass ratio of $\sim 7:1$. Using the source-plane CO($J=2 \rightarrow 1$) size of $R \sim 6$ kpc, we find a dynamical mass of $M_{\text{dyn}} \sim 8 \times 10^{10} M_\odot$ for RXJ1131. The dynamical gas mass fraction of $f_{\text{gas}} = M_{\text{gas}}/M_{\text{dyn}} \sim 19.18\%$ and baryonic gas mass fraction of $f_{\text{mol}} = M_{\text{gas}}/(M_{\text{gas}} + M_*) \sim 32.34\%$ are consistent with the trend of decreasing molecular gas content since $z \sim 2$ (e.g., Lagos et al. 2011; Tacconi et al. 2013; C13) which has been suggested as the cause for the decline in sSFR and cosmic star formation history towards $z \sim 0$ (e.g., Tacconi et al. 2013; Carilli & Walter 2013; Genzel et al. 2015). The CO-based dynamical mass ratio of $\sim 24:1$ between RXJ1131 and the companion, and a gas mass ratio of $\sim 7:1$ suggest that the system is a gas-rich, “wet” minor merger.

Fitting dust SED models to the IR-to-mm photometry, we derive a lensing-corrected dust mass of $M_{\text{dust}} \sim 4.3 \times 10^8 M_\odot$, an infrared luminosity of $L_{\text{IR}} \sim 1.5 \times 10^{12} (5.5/\mu_L) L_\odot$, and a far-IR luminosity that corresponds to a $\text{SFR}_{\text{FIR}} \sim 120 M_\odot \text{ yr}^{-1}$. These physical properties suggest that the merger system is dusty in nature with on-going star formation activity occurring at a rate comparable to local ULIRGs/mergers and high- z massive disk galaxies (da Cunha et al. 2010; Daddi et al. 2010). We also derive a stellar mass of $M_* \sim 3 \times 10^{10} M_\odot$ by fitting SED models to the rest-frame UV-to-mm photometry, which have been corrected for their respective magnification factors before performing the fit to account for differential lensing effect.

The source-plane distribution of the gas and stellar populations of different ages indicates that the CO gas is of similar spatial extent as the old and long-lasting stellar populations, whereas regions of recent star formation may

be embedded within the molecular gas reservoir as a result of gas accumulation driven by interactions with the companion. Based on dynamical mass constraints, we cannot rule out the possibility that the compact star formation in the host galaxy may be heavily dust-obscured. Hence, the true extent of recent star formation may be as extended as the molecular gas reservoir. While properties such as CO linewidth, SFR, and gas mass found in RXJ1131 are consistent with those of local ULIRGs and high- z starburst galaxies, its SFE is comparable to those of nearby and high- z disk galaxies rather than starburst systems. This is in good agreement with its disk-like kinematic signatures and its extended molecular gas distribution. We find a specific star formation rate (sSFR $\sim 4 \text{ Gyr}^{-1}$) that is $\lesssim 1.5\sigma$ higher than those of “main sequence” galaxies. The slight elevation in sSFR over the main sequence suggests that the on-going star formation activity in RXJ1131 could be enhanced by interactions with the companion. Recent simulations have illustrated that the disk component of a gas-rich progenitor galaxy with low SFE can be retained upon merging since the efficiency at removing angular momentum of the gas via gravitational torques provided by stellar components is reduced in such a system (Springel & Hernquist 2005; Robertson et al. 2006; Hopkins et al. 2009). As such, the extended gas disk of RXJ1131 together with its low SFE may indicate that the star formation in RXJ1131 could form a larger stellar bulge in the merger remnant upon coalescing.

Using the CO redshift as systemic redshift for the host galaxy of RXJ1131, we find that the redshift inferred from NLR lines reported in previous studies are consistent with this systemic redshift but the optical BLR lines are redshifted by $\sim 780 \text{ km s}^{-1} \sim 715 \text{ km s}^{-1}$. ~~This implies that the AGN is offset from the dynamical center of its host galaxy. One explanation could be that the BLRs are gravitationally bound to the central AGN, whereas this condition is not necessary for NLRs. Since the velocity offset between emission lines of the BLR and the NLR is typically $\sim 100 \pm 270 \text{ km s}^{-1}$, we thus raise an alternative explanation of a recoiling black hole in RXJ1131, which would also explain the high spin parameter reported by Reis et al. (2014).~~

Adopting the stellar mass as an upper limit to the bulge mass, we find a $M_{\text{BH}}/M_{\text{bulge}} > 0.27^{+11}_{-8} \% \mathbf{0.27^{+0.11}_{-0.08} \%}$ for RXJ1131, providing a direct constraint on the empirical $M_{\text{BH}}-M_{\text{bulge}}$ relation at $z \sim 0.65$. The elevated $M_{\text{BH}}/M_{\text{bulge}}$ ratio compared to the local relation suggests that the black hole in RXJ1131 has grown faster or earlier than its host galaxy than nearby AGN host galaxies, consistent with the results from existing studies of the evolution in the growth of SMBHs and their host galaxies (e.g., Walter et al. 2004; Peng et al. 2006; McLure et al. 2006). The elevated ratio also suggests that the stellar bulge component of RXJ1131 is still assembling in order to evolve onto the local $M_{\text{BH}}-M_{\text{bulge}}$ relation.

We thank the referee for providing detailed and constructive comments that helped improved the clarify of this manuscript. DR and RP acknowledge support from the

National Science Foundation under grant number AST-1614213 to Cornell University. RP acknowledges support through award SOSPA3-008 from the NRAO. DR acknowledges the hospitality at the Aspen Center for Physics and the Kavli Institute for Theoretical Physics during part of the writing of this manuscript. This work is based on observations carried out under project number S14BX with the IRAM NOEMA Interferometer. IRAM is supported by INSU/CNRS (France), MPG (Germany) and IGN (Spain). Support for CARMA construction was derived from the Gordon and Betty Moore Foundation, the Kenneth T. and Eileen L. Norris Foundation, the James S. McDonnell Foundation, the Associates of the California Institute of Technology, the University of Chicago, the states of Illinois, California, and Maryland, and the National Science Foundation. Ongoing CARMA development and operations are supported by the National Science Foundation under a cooperative agreement and by the CARMA consortium universities. The National Radio Astronomy Observatory is a facility of the National Science Foundation operated under cooperative agreement by Associated Universities, Inc. This research made use of data obtained with *Herschel*, an ESA space observatory with science instruments provided by European-led Principal Investigator consortia and with important participation from NASA. This research has made use of NASA's Astrophysics Data System Bibliographic Services. This work is based in part on observations made with the NASA/ESA Hubble Space Telescope, and obtained from the Hubble Legacy Archive, which is a collaboration between the Space Telescope Sci-

ence Institute (STScI/NASA), the Space Telescope European Coordinating Facility (ST-ECF/ESA) and the Canadian Astronomy Data Centre (CADC/NRC/CSA). This work is based in part on observations made with the *Spitzer Space Telescope*, which is operated by the Jet Propulsion Laboratory, California Institute of Technology under a contract with NASA. This publication made use of data products from the Wide-field Infrared Survey Explorer, which is a joint project of the University of California, Los Angeles, and the Jet Propulsion Laboratory/California Institute of Technology, funded by the National Aeronautics and Space Administration. This publication made use of data products from the Two Micron All Sky Survey, which is a joint project of the University of Massachusetts and the Infrared Processing and Analysis Center/California Institute of Technology, funded by the National Aeronautics and Space Administration and the National Science Foundation. This research made use of the NASA/IPAC Extragalactic Database (NED) which is operated by the Jet Propulsion Laboratory, California Institute of Technology, under contract with the National Aeronautics and Space Administration. This research made use of Astropy, a community-developed core Python package for Astronomy (Astropy Collaboration et al. 2013). This research made use of APLpy, an open-source plotting package for Python hosted at <http://aplpy.github.com>.

Facilities: IRAM PdBI, CARMA, VLA, *Herschel*(SPIRE), WISE, IRAS, 2MASS, *Spitzer*(IRAC, MIPS), HST(ACS, NICMOS)

Alexander, D. M., Smail, I., Bauer, F. E., et al. 2005, *Nature*, **434**, 738
 Alexander, D. M., Brandt, W. N., Smail, I., et al. 2008, *AJ*, **135**, 1968
 Astropy Collaboration, Robitaille, T. P., Tollerud, E. J., et al. 2013, *A&A*, **558**, A33
 Bonning, E. W., Shields, G. A., & Salvander, S. 2007, *ApJ*, **666**, L13
 Borys, C., Smail, I., Chapman, S. C., et al. 2005, *ApJ*, **635**, 853
 Bothwell, M. S., Smail, I., Chapman, S. C., et al. 2013, *MNRAS*, **429**, 3047
 Brewer, B. J., & Lewis, G. F. 2008, *MNRAS*, **390**, 39
 Bruzual, G., & Charlot, S. 2003, *MNRAS*, **344**, 1000
 Bussmann, R. S., Leung, T. K. D., & Conley, A. 2015a
 Bussmann, R. S., Riechers, D., Fialkov, A., et al. 2015b, *ApJ*, **812**, 43
 Campanelli, M., Lousto, C. O., Zlochower, Y., & Merritt, D. 2007, *Physical Review Letters*, **98**, 231102
 Carilli, C. L., & Walter, F. 2013, *ARA&A*, **51**, 105
 Civano, F., Elvis, M., Lanzuisi, G., et al. 2010, *ApJ*, **717**, 209
 Claeskens, J.-F., Sluse, D., Riaud, P., & Surdej, J. 2006, *A&A*, **451**, 865
 Combes, F., García-Burillo, S., Braine, J., et al. 2011, *A&A*, **528**, A124
 —, 2013, *A&A*, **550**, A41
 Coppin, K. E. K., Swinbank, A. M., Neri, R., et al. 2008, *MNRAS*, **389**, 45
 Courteau, S. 1997, *AJ*, **114**, 2402
 Courteau, S., & Rix, H.-W. 1997, in Bulletin of the American Astronomical Society, Vol. 29, American Astronomical Society Meeting

Abstracts, 1332
 da Cunha, E., Charlot, S., & Elbaz, D. 2008, *MNRAS*, **388**, 1595
 da Cunha, E., Charmandaris, V., Díaz-Santos, T., et al. 2010, *A&A*, **523**, A78
 da Cunha, E., Walter, F., Smail, I. R., et al. 2015, *ApJ*, **806**, 110
 Daddi, E., Dannerbauer, H., Elbaz, D., et al. 2008, *ApJ*, **673**, L21
 Daddi, E., Bournaud, F., Walter, F., et al. 2010, *ApJ*, **713**, 686
 Dannerbauer, H., Daddi, E., Riechers, D. A., et al. 2009, *ApJ*, **698**, L178
 Decarli, R., Dotti, M., Mazzucchelli, C., Montuori, C., & Volonteri, M. 2014, *MNRAS*, **445**, 1558
 Di Matteo, T., Springel, V., & Hernquist, L. 2005, *Nature*, **433**, 604
 Dowell, C. D., Conley, A., Glenn, J., et al. 2014, *ApJ*, **780**, 75
 Downes, D., & Solomon, P. M. 1998, *ApJ*, **507**, 615
 Draine, B. T., Dale, D. A., Bendo, G., et al. 2007, *ApJ*, **663**, 866
 Dunne, L., Eales, S. A., & Edmunds, M. G. 2003, *MNRAS*, **341**, 589
 Dye, S., Furlanetto, C., Swinbank, A. M., et al. 2015, *MNRAS*, **452**, 2258
 Erb, D. K., Steidel, C. C., Shapley, A. E., et al. 2006, *ApJ*, **646**, 107
 Fazio, G. G., Hora, J. L., Allen, L. E., et al. 2004, *ApJS*, **154**, 10
 Gao, Y., & Solomon, P. M. 1999, *ApJ*, **512**, L99
 —, 2004, *ApJS*, **152**, 63
 Geach, J. E., Smail, I., Moran, S. M., et al. 2011, *ApJ*, **730**, L19
 Genzel, R., Tacconi, L. J., Lutz, D., et al. 2015, *ApJ*, **800**, 20
 Greve, T. R., Bertoldi, F., Smail, I., et al. 2005, *MNRAS*, **359**, 1165
 Häring, N., & Rix, H.-W. 2004, *ApJ*, **604**, L89
 Hinshaw, G., Larson, D., Komatsu, E., et al. 2013, *ApJS*, **208**, 19
 Hopkins, A. M., & Beacom, J. F. 2006, *ApJ*, **651**, 142
 Hopkins, P. F., Cox, T. J., Younger, J. D., & Hernquist, L. 2009, *ApJ*,

- 691, 1168
 Hopkins, P. F., Hernquist, L., Cox, T. J., et al. 2006, *ApJS*, **163**, 1
 Ivison, R. J., Papadopoulos, P. P., Smail, I., et al. 2011, *MNRAS*, **412**, 1913
 Kennicutt, Jr., R. C. 1998, *ARA&A*, **36**, 189
 Komossa, S., Zhou, H., & Lu, H. 2008, *ApJ*, **678**, L81
 Lagos, C. D. P., Baugh, C. M., Lacey, C. G., et al. 2011, *MNRAS*, **418**, 1649
 Lamastra, A., Menci, N., Fiore, F., et al. 2013, *A&A*, **559**, A56
 Li, A., & Draine, B. T. 2001, *ApJ*, **554**, 778
 Loeb, A. 2007, *Physical Review Letters*, **99**, 041103
 Madau, P., & Dickinson, M. 2014, *ARA&A*, **52**, 415
 Madau, P., & Quataert, E. 2004, *ApJ*, **606**, L17
 Magorrian, J., Tremaine, S., Richstone, D., et al. 1998, *AJ*, **115**, 2285
 McLure, R. J., Jarvis, M. J., Targett, T. A., Dunlop, J. S., & Best, P. N. 2006, *MNRAS*, **368**, 1395
 Miller, S. H., Bundy, K., Sullivan, M., Ellis, R. S., & Treu, T. 2011, *ApJ*, **741**, 115
 Narayanan, D., Krumholz, M. R., Ostriker, E. C., & Hernquist, L. 2012, *MNRAS*, **421**, 3127
 Nelson, C. H. 2000, *ApJ*, **544**, L91
 Neugebauer, G., Habing, H. J., van Duinen, R., et al. 1984, *ApJ*, **278**, L1
 Ott, S. 2010, in *Astronomical Society of the Pacific Conference Series*, Vol. 434, *Astronomical Data Analysis Software and Systems XIX*, ed. Y. Mizumoto, K.-I. Morita, & M. Ohishi, 139
 Page, M. J., Symeonidis, M., Vieira, J. D., et al. 2012, *Nature*, **485**, 213
 Papadopoulos, P. P., van der Werf, P., Xilouris, E., Isaak, K. G., & Gao, Y. 2012, *ApJ*, **751**, 10
 Peng, C. Y., Impey, C. D., Rix, H.-W., et al. 2006, *ApJ*, **649**, 616
 Pooley, D., Blackburne, J. A., Rappaport, S., & Schechter, P. L. 2007, *ApJ*, **661**, 19
 Puech, M., Flores, H., Hammer, F., et al. 2008, *A&A*, **484**, 173
 Reis, R. C., Reynolds, M. T., Miller, J. M., & Walton, D. J. 2014, *Nature*, **507**, 207
 Richards, G. T., Vanden Berk, D. E., Reichard, T. A., et al. 2002, *AJ*, **124**, 1
 Riechers, D. A., Hodge, J., Walter, F., Carilli, C. L., & Bertoldi, F. 2011, *ApJ*, **739**, L31
 Riechers, D. A., Walter, F., Brewer, B. J., et al. 2008, *ApJ*, **686**, 851
 Riechers, D. A., Bradford, C. M., Clements, D. L., et al. 2013, *Nature*, **496**, 329
 Rieke, G. H., Young, E. T., Engelbracht, C. W., et al. 2004, *ApJS*, **154**, 25
 Robertson, B., Bullock, J. S., Cox, T. J., et al. 2006, *ApJ*, **645**, 986
 Rybak, M., McKean, J. P., Vegetti, S., Andreani, P., & White, S. D. M. 2015, *MNRAS*, **451**, L40
 Saintonge, A., Kauffmann, G., Kramer, C., et al. 2011, *MNRAS*, **415**, 32
 Sajina, A., Yan, L., Fadda, D., Dasyra, K., & Huynh, M. 2012, *ApJ*, **757**, 13
 Salpeter, E. E. 1955, *ApJ*, **121**, 161
 Simpson, J. M., Smail, I., Swinbank, A. M., et al. 2012, *MNRAS*, **426**, 3201
 Skrutskie, M. F., Cutri, R. M., Stiening, R., et al. 2006, *AJ*, **131**, 1163
 Sluse, D., Claeskens, J.-F., Hutsemékers, D., & Surdej, J. 2007, *A&A*, **468**, 885
 Sluse, D., Hutsemékers, D., Courbin, F., Meylan, G., & Wambsgans, J. 2012, *A&A*, **544**, A62
 Sluse, D., Surdej, J., Claeskens, J.-F., et al. 2003, *A&A*, **406**, L43
 Solomon, P. M., Downes, D., Radford, S. J. E., & Barrett, J. W. 1997, *ApJ*, **478**, 144
 Solomon, P. M., & Vanden Bout, P. A. 2005, *ARA&A*, **43**, 677
 Springel, V., & Hernquist, L. 2005, *ApJ*, **622**, L9
 Steinhardt, C. L., Schramm, M., Silverman, J. D., et al. 2012, *ApJ*, **759**, 24
 Stern, D., Eisenhardt, P., Gorjian, V., et al. 2005, *ApJ*, **631**, 163
 Tacconi, L. J., Neri, R., Chapman, S. C., et al. 2006, *ApJ*, **640**, 228
 Tacconi, L. J., Genzel, R., Smail, I., et al. 2008, *ApJ*, **680**, 246
 Tacconi, L. J., Neri, R., Genzel, R., et al. 2013, *ApJ*, **768**, 74
 Toomre, A., & Toomre, J. 1972, *ApJ*, **178**, 623
 Ueda, J., Iono, D., Yun, M. S., et al. 2014, *ApJS*, **214**, 1
 Vrtillek, J. M. 1985, *ApJ*, **294**, 121
 Walter, F., Carilli, C., Bertoldi, F., et al. 2004, *ApJ*, **615**, L17
 Walter, F., Decarli, R., Sargent, M., et al. 2014, *ApJ*, **782**, 79
 Weiß, A., Downes, D., Walter, F., & Henkel, C. 2007, **375**, 25
 Wilson, C. D., Petitpas, G. R., Iono, D., et al. 2008, *ApJS*, **178**, 189
 Wright, E. L., Eisenhardt, P. R. M., Mainzer, A. K., et al. 2010, *AJ*, **140**, 1868
 Zubko, V., Dwek, E., & Arendt, R. G. 2004, *ApJS*, **152**, 211